

Ground-based near-UV observations of 15 transiting exoplanets: constraints on their atmospheres and no evidence for asymmetrical transits

Jake D. Turner,^{1,2★} Kyle A. Pearson,³ Lauren I. Biddle,³ Brianna M. Smart,^{3,4} Robert T. Zellem,¹ Johanna K. Teske,^{3†} Kevin K. Hardegree-Ullman,^{3,5} Caitlin C. Griffith,¹ Robin M. Leiter,² Ian T. Cates,³ Megan N. Nieberding,³ Carter-Thaxton W. Smith,³ Robert M. Thompson,³ Ryan Hofmann,³ Michael P. Berube,³ Chi H. Nguyen,³ Lindsay C. Small,³ Blythe C. Guvenen,⁶ Logan Richardson,⁷ Allison McGraw,³ Brandon Raphael,³ Benjamin E. Crawford,³ Amy N. Robertson,³ Ryan Tombleson,³ Timothy M. Carleton,⁸ Allison P.M. Towner,³ Amanda M. Walker-LaFollette,³ Jeffrey R. Hume,³ Zachary T. Watson,³ Christen K. Jones,³ Matthew J. Lichtenberger,³ Shelby R. Hoglund,³ Kendall L. Cook,³ Cory A. Crossen,³ Curtis R. Jorgensen,³ James M. Romine,³ Alejandro R. Thompson,³ Christian F. Villegas,³ Ashley A. Wilson,³ Brent Sanford,³ Joanna M. Taylor⁹ and Triana N. Henz³

Affiliations are listed at the end of the paper

Accepted 2016 March 8. Received 2016 March 8; in original form 2015 June 22

ABSTRACT

Transits of exoplanets observed in the near-UV have been used to study the scattering properties of their atmospheres and possible star–planet interactions. We observed the primary transits of 15 exoplanets (CoRoT-1b, GJ436b, HAT-P-1b, HAT-P-13b, HAT-P-16b, HAT-P-22b, TrES-2b, TrES-4b, WASP-1b, WASP-12b, WASP-33b, WASP-36b, WASP-44b, WASP-48b, and WASP-77Ab) in the near-UV and several optical photometric bands to update their planetary parameters, ephemerides, search for a wavelength dependence in their transit depths to constrain their atmospheres, and determine if asymmetries are visible in their light curves. Here, we present the first ground-based near-UV light curves for 12 of the targets (CoRoT-1b, GJ436b, HAT-P-1b, HAT-P-13b, HAT-P-22b, TrES-2b, TrES-4b, WASP-1b, WASP-33b, WASP-36b, WASP-48b, and WASP-77Ab). We find that none of the near-UV transits exhibit any non-spherical asymmetries, this result is consistent with recent theoretical predictions by Ben-Jaffel et al. and Turner et al. The multiwavelength photometry indicates a constant transit depth from near-UV to optical wavelengths in 10 targets (suggestive of clouds), and a varying transit depth with wavelength in 5 targets (hinting at Rayleigh or aerosol scattering in their atmospheres). We also present the first detection of a smaller near-UV transit depth than that measured in the optical in WASP-1b and a possible opacity source that can cause such radius variations is currently unknown. WASP-36b also exhibits a smaller near-UV transit depth at

* E-mail: jt6an@virginia.edu

† Currently an Origins Fellow at Carnegie DTM/OCIW.

2.6σ . Further observations are encouraged to confirm the transit depth variations seen in this study.

Key words: techniques: photometric – planets and satellites: atmospheres – planet–star interactions.

1 INTRODUCTION

Near-ultraviolet (near-UV) transits of short-period exoplanets are a great tool to study star–planet interactions (e.g. tidal, gravitational, magnetic) and the scattering properties of their atmospheres (e.g. Fossati et al. 2015). The atmospheres of hot Jovian exoplanets in the near-UV (300–450 nm) can be dominated by Rayleigh scattering, other forms of scattering or absorption, or clouds/hazes (Seager & Sasselov 2000; Brown 2001; Benneke & Seager 2012; Benneke & Seager 2013; Griffith 2014). Clouds reduce the strength of spectral features thus causing the transit depth from near-UV to optical to be constant (Seager & Sasselov 2000; Brown 2001; Gibson et al. 2013b; Knutson et al. 2014; Kreidberg et al. 2014), and the Rayleigh scattering signature causes the transit depth to increase in the near-UV (Lecavelier Des Etangs et al. 2008; Tinetti et al. 2010; de Wit & Seager 2013; Griffith 2014). Additionally, near-UV transits may exhibit asymmetries in their light curves such as ingress/egress timing differences, asymmetric transit shapes, longer durations, or significantly deeper transit depths (>1 per cent) than the optical (e.g. Vidal-Madjar et al. 2003; Fossati et al. 2010; Ehrenreich et al. 2012; Kulow et al. 2014). The physical interpretations of these abnormalities vary, and include bow shocks, tidal interactions, star–planet magnetic interactions, a plasma torus originating from an active satellite, or escaping planetary atmospheres (e.g. Lai, Helling & van den Heuvel 2010; Vidotto, Jardine & Helling 2010; Ben-Jaffel & Ballester 2014; Matsakos, Uribe & Königl 2015).

There are 19 exoplanets with ground- or space-based observations in the UV (100–450 nm). These observations can be subdivided into two groups: asymmetric and symmetric light curves. There are five exoplanets (55 Cnc b, GJ 436b, HD 189733b, HD 209458b, WASP-12b) where asymmetries in their light curves are observed (Vidal-Madjar et al. 2003, 2004, 2008, 2013; Ben-Jaffel 2007, 2008; Fossati et al. 2010; Ehrenreich et al. 2012, 2015; Haswell et al. 2012; Ben-Jaffel & Ballester 2013; Kulow et al. 2014; Nichols et al. 2015). For the symmetric transits, nine hot Jupiters (HAT-P-1b, HAT-P-12b, HAT-P-16b, TrES-3b, WASP-12b, WASP-17b, WASP-19b, WASP-43b, WASP-39b) are observed to have a constant planetary radii from near-UV to optical wavelengths (Copperwheat et al. 2013; Turner et al. 2013; Bento et al. 2014; Nikolov et al. 2014; Pearson, Turner & Sagan 2014; Mallonn et al. 2015; Ricci et al. 2015; Sing et al. 2016). Additionally, 11 exoplanets with symmetric light curves (GJ 3470b, HD 189733b, HD 209458b, HAT-P-5b, HAT-P-12b, WASP-6b, WASP-12b, WASP-17b, WASP-31b, WASP-39b, XO-2b) are observed to have a larger near-UV radii than optical wavelengths (Lecavelier Des Etangs et al. 2008; Sing et al. 2008, 2011, 2013, 2015, 2016; Southworth et al. 2012b; Nascimbeni et al. 2013; Zellem et al. 2015). There seems to be a wavelength distinction between asymmetric and symmetric lights where asymmetric transits are only observed below 300 nm. However, recent observations of asymmetric transits at optical wavelengths (Rappaport et al. 2012, 2014; van Werkhoven et al. 2014; Cabrera et al. 2015; Cauley et al. 2015) hint that this dichotomy might not be the case.

In this study, we investigate whether ground-based near-UV observations exhibit asymmetries. Most notably, it was predicted that

a transiting exoplanet can potentially show an earlier transit ingress in the UV than in the optical, while the transit egress times will be unaffected due to the early absorption of star light due to a bow shock (Vidotto, Jardine & Helling 2010, 2011b,c; Llama et al. 2011, 2013; Vidotto et al. 2011a). Additionally, the near-UV transit will have a greater drop in flux than the optical transit and will no longer be symmetric about the mid-transit time (Llama et al. 2011, 2013; Vidotto et al. 2011c). This effect is explained by the presence of a bow shock on the leading edge of the planet formed by interactions between the planet’s magnetosphere and the stellar coronal plasma. If the shocked material in the magnetosheath becomes sufficiently opaque, it will absorb starlight and cause an early ingress in the near-UV light curve (Vidotto et al. 2011c, see fig. 6). Vidotto et al. (2011b, hereafter *VJH11a*) predict that near-UV ingress asymmetries should be common in transiting exoplanets and tabulated a list of the 69 targets that should exhibit this effect.

Is it possible to observe near-UV asymmetries from the ground? Previous observations of an early ingress on WASP-12b and HD 189733b observe a flux drop difference of about ~ 1 per cent and a timing difference of ~ 30 min between the near-UV and optical light curves (Fossati et al. 2010; Haswell et al. 2012; Ben-Jaffel & Ballester 2013; Nichols et al. 2015). Both these properties are well within reach for ground-based metre-sized telescopes (e.g. Copperwheat et al. 2013; Turner et al. 2013; Pearson et al. 2014), like the Steward Observatory 1.55-m Kuiper Telescope used for the near-UV observations in this study. Additionally, Nichols et al. (2015) find that summing over the entire NUV band (253.9–281.1 nm) on *Hubble Space Telescope* (*HST*) still resulted in an early ingress, which they attributed to a blend of thousands of lines of metals (e.g. Mg, Na, Fe, Al, Co, Al Mn). Therefore, ground-based broadband near-UV observations (303–417 nm) might also experience an early near-UV ingress by the blending of lots of lines from the same metal species that exist at *HST* wavelengths (e.g. Na I/II , Ca II/III , Na I , Mg I , Al I , Mn I/II , Fe I/II , Co I/II ; Morton 1991, 2000; Sansonetti 2005). Therefore, it is feasible to observe near-UV asymmetries from the ground by taking all the factors discussed above into consideration.

However, recent studies by Ben-Jaffel & Ballester (2014) and Turner et al. (2016) cast doubt on observing asymmetries in all ground- and space-based UV wavelengths using the *VJH11a* bow shock model. Ben-Jaffel & Ballester (2014) use simple recombination and ionization equilibrium calculations for realistic parameters of the stellar corona ($T \sim 10^6$ K; Aschwanden 2005) to determine that only highly ionized stages of heavy elements can cause any detectable optical depth. Furthermore, Turner et al. (2016) use the plasma photoionization and microphysics code *CLOUDY* (Ferland et al. 1998, 2013) to investigate all opacity sources at UV and optical wavelengths that could cause an early ingress due to the presence of a bow shock compressing the coronal plasma. Turner et al. (2016) also find that the optical depths in the compressed stellar wind ($T \sim 10^6$ K; Aschwanden 2005, $n \sim 10^4$ cm $^{-3}$; McKenzie, Axford & Banaszkiewicz 1997) are orders of magnitude too small ($> 3 \times 10^{-7}$) to cause an observable absorption in space- and ground-based UV and optical observations (even for stellar wind densities 10^4 times higher than what is expected).

Table 1. Comparison of the planetary systems in this study.^a References. – (c) Knutson, Howard & Isaacson (2010); (d) Pont et al. (2010); (e) Johnson et al. (2008); (f) Winn et al. (2010); (g) Moutou et al. (2011); (h) Winn et al. (2008b); (i) Narita et al. (2010); (j) Albrecht et al. (2011); (k) Albrecht et al. (2012); (l) Collier Cameron et al. (2010).

Planet name	M_p (M_{Jup})	R_p (R_{Jup})	a (au)	P_p (d)	Spec. type	M_* (M_\odot)	R_* (R_\odot)	[Fe/H]	$\log(R'_{hk})(c)$	λ^b ($^\circ$)
CoRoT-1b	1.03	1.49	0.025	1.51	G0V	0.95	1.11	−0.30	−5.132	77(d)
GJ346b	0.072	0.38	0.029	2.63	M2.5V	0.45	0.46	−0.32	−5.298	–
HAT-P-1b	0.53	1.24	0.055	4.47	G0V	1.13	1.14	0.13	−4.984	3.7(e)
HAT-P-13b	0.85	1.28	0.043	2.92	G4	1.22	1.56	0.43	−5.134	1.9(f)
HAT-P-16b	4.2	1.29	0.041	2.78	F8	1.22	1.24	0.17	−4.864	−10(g)
HAT-P-22b	2.15	1.08	0.041	3.21	G5	0.92	1.04	0.22	–	–
TrES-2b	1.19	1.22	0.036	2.47	G0V	0.98	1.0	−0.15	−4.949	−9(h)
TrES-4b	0.91	1.78	0.051	3.55	F	1.39	1.82	0.14	−5.104	6.3(i)
WASP-1b	1.03	1.49	0.025	1.51	F7V	0.95	1.11	−0.30	−5.114	−59(j)
WASP-12b	1.35	1.79	0.023	1.09	G0	1.28	1.63	0.30	−5.500	63(k)
WASP-33b	1.76	1.50	0.026	1.22	A5	1.5	1.44	0.1	–	251.6(l)
WASP-36b	2.26	1.27	0.026	1.54	G2	1.02	0.94	−0.31	–	–
WASP-44b	0.89	1.14	0.035	2.42	G8V	0.95	0.93	0.06	–	–
WASP-48b	0.97	1.67	0.034	2.14	G	1.19	1.75	−0.12	–	–
WASP-77Ab	1.76	1.21	0.024	1.36	G8V	1.0	0.96	0.1	–	–

^aInformation about the systems is obtained from the Exoplanet Data Explorer at exoplanets.org (Wright et al. 2011).

^b λ is the angle between the sky projections of the planetary orbital axis and the stellar rotation axis.

The goals of this paper are to study the atmospheres of 15 transiting exoplanet targets and to determine whether ground-based near-UV transit observations are sensitive to light-curve asymmetries. Our data can be used to confirm the predictions by Ben-Jaffel & Ballester (2014) and Turner et al. (2016) that an early ingress should not be present in ground-based near-UV transits. Our sample is chosen to contain a wide variety of different system parameters to determine if any system parameters correlate with the existence of a bow shock (Table 1). We also perform follow-up ground-based near-UV observations of WASP-12b (Copperwheat et al. 2013) and HAT-P-16b (Pearson et al. 2014). Using our data set, we update the planetary system parameters (Section 4), present a new ephemeris to aid in future observations (Section 4.1), and search for a wavelength dependence in the planetary radii that can be used to constrain their atmospheric compositions (Section 6.2).

2 OBSERVATIONS AND DATA REDUCTION

All of our observations were conducted at the University of Arizona’s Steward Observatory 1.55-m (61 inches) Kuiper Telescope on Mt. Bigelow near Tucson, Arizona, using the Mont4k CCD. The Mont4k CCD contains a 4096×4096 pixel sensor with a field of view of $9.7 \text{ arcmin} \times 9.7 \text{ arcmin}$. We used 3×3 binning to achieve a resolution of $0.43 \text{ arcsec pixel}^{-1}$ and shorten our read-out time to $\sim 10 \text{ s}$. Our observations were taken with the Bessell U (303–417 nm), Harris B (360–500 nm), Harris V (473–686 nm), and Harris R (550–900 nm) photometric band filters. Specifically, the Bessell U filter is a near-UV filter and has a transmission peak of 70 per cent near 370 nm. To ensure accurate timing in these observations, the clocks were synchronized with an NTP time server every few seconds. In all the data sets, the average shift in the centroid of our targets is less than 1 pixel (0.43 arcsec) due to excellent autoguiding (the max is 3 pixels), which minimizes our need to worry about intrapixel sensitivity. Seeing ranged from 0.86–4.12 arcsec throughout our complete set of observations. A summary of all our observations is displayed in Table 2.

To reduce the data, we use the automated reduction pipeline EXODRPL¹ which generates a series of IRAF² scripts that calibrate images using standard reduction procedures and perform aperture photometry (Pearson et al. 2014). Each of our images is bias-subtracted and flat-fielded. Turner et al. (2013) determined that using more than 10 flat-field images in the reduction of Kuiper/Mont4k data does not significantly reduce the noise in the resulting images. To optimize telescope time, we use 10 flats and 10 bias frames in all of our observations and reductions.

To produce the light curve for each observation, we perform aperture photometry (using the task PHOT in the IRAF DAOPHOT package) by measuring the flux from our target star as well as the flux from up to eight different reference stars with 110 different circular aperture radii. We insure that each reference star is not a variable star by checking the Aladin Sky Atlas,³ the International Variable Star Index,⁴ and by examining their light curves divided by the average of the other reference stars. The aperture radii sizes we explore differ for every observation due to changes in seeing conditions. For the analysis, we use a constant sky annulus for every night of observation of each target (a different sky annulus is used depending on the seeing for each date and the crowdedness of the field for each target). The sky analysis is chosen to be a radius greater than the target aperture so that no stray light from the target star is included. We also make sure that no other stars fall in the chosen sky annulus. A synthetic light curve is produced by averaging the light curves of the reference stars. Then, the final transit light curve of each date is normalized by dividing by this synthetic light curve to correct for systematics due to atmospheric variations and airmass differences throughout the observations. Every combination of reference stars and aperture radii are considered. We systematically choose the

¹ <https://sites.google.com/a/email.arizona.edu/kyle-pearson/exodrpl>

² IRAF is distributed by the National Optical Astronomy Observatory, which is operated by the Association of Universities for Research in Astronomy, Inc., under cooperative agreement with the National Science Foundation.

³ <http://aladin.u-strasbg.fr/>; Bonnarel et al. (2000).

⁴ <http://www.aavso.org/vsx>

Table 2. Journal of observations.

Planet name	Date (UT)	Filter ^a	Cadence (s)	OoT rms ^b (mmag)	Res rms ^c (mmag)	Seeing (arcsec)	χ_r^{2d}
CoRoT-1b	2012 December 06	<i>U</i>	70	3.59	3.95	1.46–2.95	0.49
GJ436b	2012 March 23	<i>U</i>	60	2.96	2.85	0.96–1.99	0.68
"	2012 April 07	<i>U</i>	61	2.83	2.70	1.22–2.10	1.37
HAT-P-1b	2012 October 02	<i>U</i>	40	1.44	1.45	1.57–2.00	1.69
HAT-P-13b	2013 March 02	<i>U</i>	58	1.91	1.63	1.67–2.89	1.76
HAT-P-16b	2013 November 02	<i>U</i>	55	2.50	2.50	1.40–3.98	1.23
HAT-P-22b	2013 February 22	<i>U</i>	70	3.42	3.17	1.41–4.12	0.26
"	2013 March 22	<i>U</i>	71	2.07	2.12	1.34–2.26	1.16
TrES-2b	2012 October 29	<i>U</i>	50	3.05	2.54	1.36–2.53	1.27
TrES-4b	2011 July 26	<i>U</i>	116	4.42	4.08	1.29–3.05	3.65
"	2011 July 26	<i>R</i>	116	5.54	3.93	1.29–3.05	2.09
WASP-1b	2013 September 19	<i>U</i>	133	2.92	3.31	1.10–2.98	1.56
"	2013 September 19	<i>B</i>	135	2.80	2.36	1.10–2.98	3.61
"	2013 October 22	<i>U</i>	137	1.58	1.79	1.21–2.64	1.06
"	2013 October 22	<i>B</i>	136	1.23	1.25	1.21–2.64	1.60
WASP-12b	2011 November 15	<i>R</i>	126	1.40	1.47	1.72–2.10	2.14
"	2011 November 15	<i>U</i>	126	1.67	1.62	1.72–2.10	0.92
"	2012 March 22	<i>U</i>	61	2.54	2.23	1.33–2.15	0.47
"	2012 October 02	<i>U</i>	61	2.53	2.11	2.07–3.18	0.79
"	2012 November 30	<i>U</i>	55	3.30	3.61	1.45–3.24	0.94
WASP-33b	2012 October 01	<i>U</i>	27	2.57	2.60	1.12–1.99	1.54
"	2012 December 01	<i>U</i>	91	2.45	2.63	1.75–2.90	8.60
"	2012 December 01	<i>B</i>	91	7.17	6.68	1.75–2.90	1.91
WASP-36b	2012 December 29	<i>R</i>	31	1.90	2.50	1.92–2.80	1.44
"	2013 March 16	<i>U</i>	60	3.86	5.74	1.46–2.96	0.63
WASP-44b	2012 October 13	<i>U</i>	68	6.22	5.64	1.77–2.58	1.08
"	2013 October 19	<i>B</i>	116	2.33	2.50	1.07–1.95	1.19
"	2013 October 19	<i>V</i>	120	2.04	2.25	1.07–1.95	1.85
WASP-48b	2012 October 09	<i>U</i>	71	1.92	2.36	1.54–3.11	1.40
WASP-77Ab	2012 December 06	<i>U</i>	68	1.58	1.53	2.31–2.95	2.87

^aFilter: *B* is the Harris *B* (330–550 nm), *R* is the Harris *R* (550–900 nm), *V* is the Harris *V* (473–686 nm) and *U* is the Bessell *U* (303–417 nm).

^bOoT rms relative flux.

^cResidual (res) rms flux after subtracting the EXOMOP best-fitting model from the data.

^dReduced χ^2 calculated using the EXOMOP best-fitting model.

best reference stars and aperture by minimizing the scatter in the Out-of-Transit (OoT) data points. The 1σ error bars on the data points include the readout noise, the Poisson noise, and the flat-fielding errors. The final light curves are presented in Figs 1–5. The data points of all our transits are available in electronic form (see Table 3). For all the transits, the OoT baselines have a photometric root mean squared (rms) value between 1.23 and 6.22 mmag, consistent with previous high S/N transit photometry using the Mont4k on the 1.55-m Kuiper telescope (Dittmann et al. 2009b,a, 2010, 2012; Scuderi et al. 2010; Teske et al. 2013; Turner et al. 2013; Pearson et al. 2014; Zellem et al. 2015).

3 LIGHT-CURVE ANALYSIS

3.1 EXOMOP

To find the best fit to the light curves, we develop a modelling package called the EXOplanet MOdeling Package (EXOMOP; Pearson et al. 2014)⁵ that uses the analytic equations of Mandel & Agol

(2002) to generate a model transit. The χ^2 -fitting statistic for the model light curve is

$$\chi^2 = \sum_{i=1}^n \left[\frac{f_i(\text{obs}) - f_i(\text{model})}{\sigma_i(\text{obs})} \right]^2, \quad (1)$$

where n is the total number of data points, $f_i(\text{obs})$ is the observed flux at time i , $\sigma_i(\text{obs})$ is the error in the observed flux, and $f_i(\text{model})$ is the calculated model flux. The goal of the light curve modelling is to explore the solution-space effectively to determine the $f_i(\text{model})$ that minimizes χ^2 .

The Bayesian Information Criterion (BIC; Schwarz 1978) is used to assess overfitting of the data with EXOMOP. The BIC is defined as

$$\text{BIC} = \chi^2 + k \ln(n), \quad (2)$$

where χ^2 is the chi-squared calculated for the best-fitting model (equation 1), k is the number of free parameters in the model fit [$f_i(\text{model})$], and n is the number of data points in the transit. The possible free parameters in the Mandel & Agol (2002) model are the planet-to-star radius (R_p/R_*), the scaled semimajor axis (a/R_*), inclination (i), mid-transit time (T_c), linear limb darkening coefficient (μ_1), and quadratic limb darkening coefficient (μ_2). The power of the BIC is the penalty for a higher number of fitted model parameters, making it a robust way to compare different best-fitting models.

⁵EXOMOPv7.0 is used in the analysis and is available at <https://sites.google.com/site/astrojaketurner/codes>.

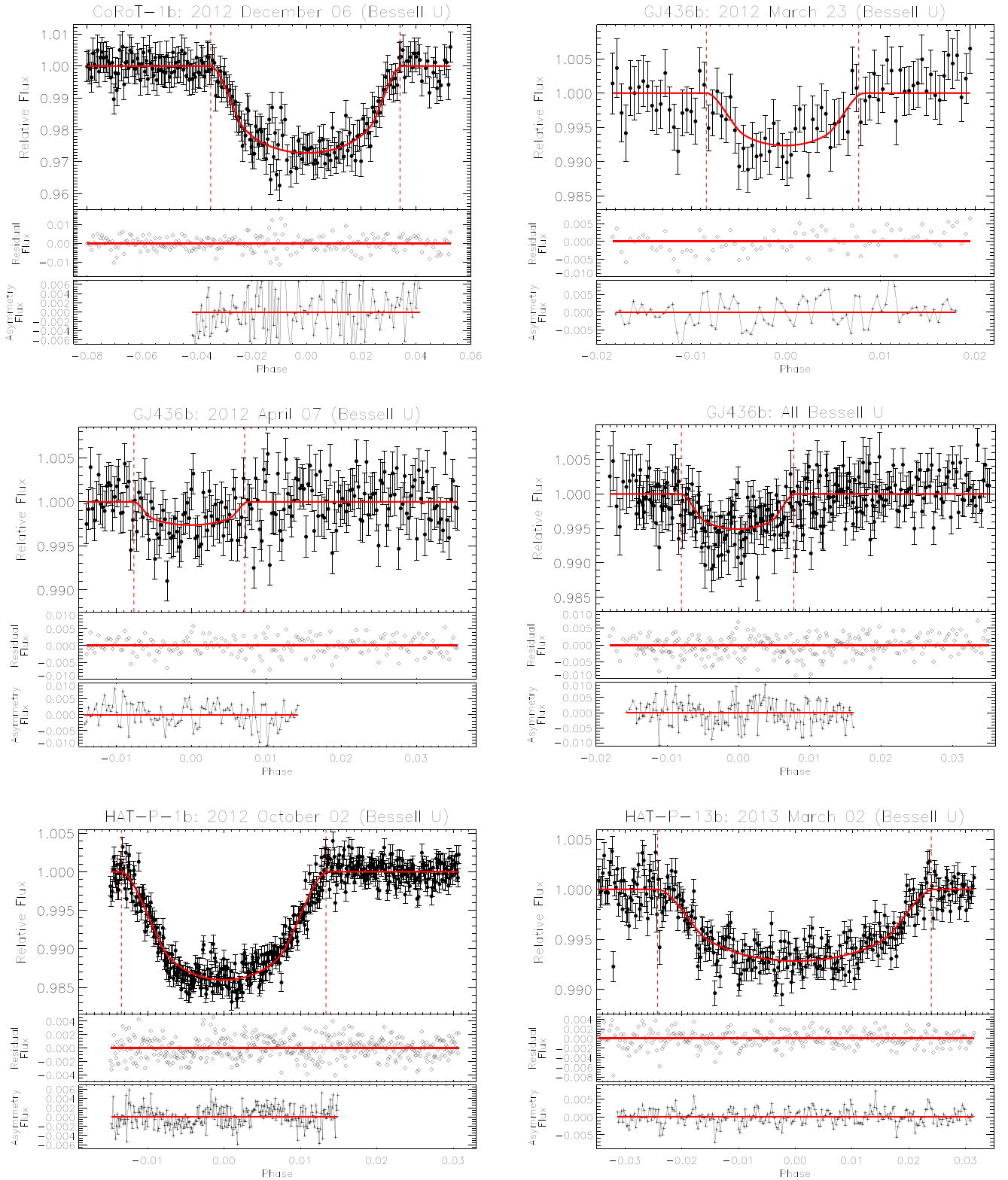


Figure 1. Light curves of CoRoT-1b, GJ436b, HAT-P-1b, and HAT-P-13b. The 1σ error bars include the readout noise, the Poisson noise, and the flat-fielding error. The best-fitting models obtained from the EXOMOP are shown as a solid red line. The EXOMOP best-fitting model predicted ingress and egress points are shown as dashed red vertical lines. The residuals (light curve – EXOMOP model) are shown in the second panel. The third panel shows the residuals of the transit subtracted by the mirror image of itself (Section 3.1.3). See Table 2 for the cadence, OoT rms flux, and residual rms flux for each light curve. We do not observe an early ingress or any non-spherical asymmetries in any of the near-UV transits. The data points for all the transits are available in electronic form (see Table 3).

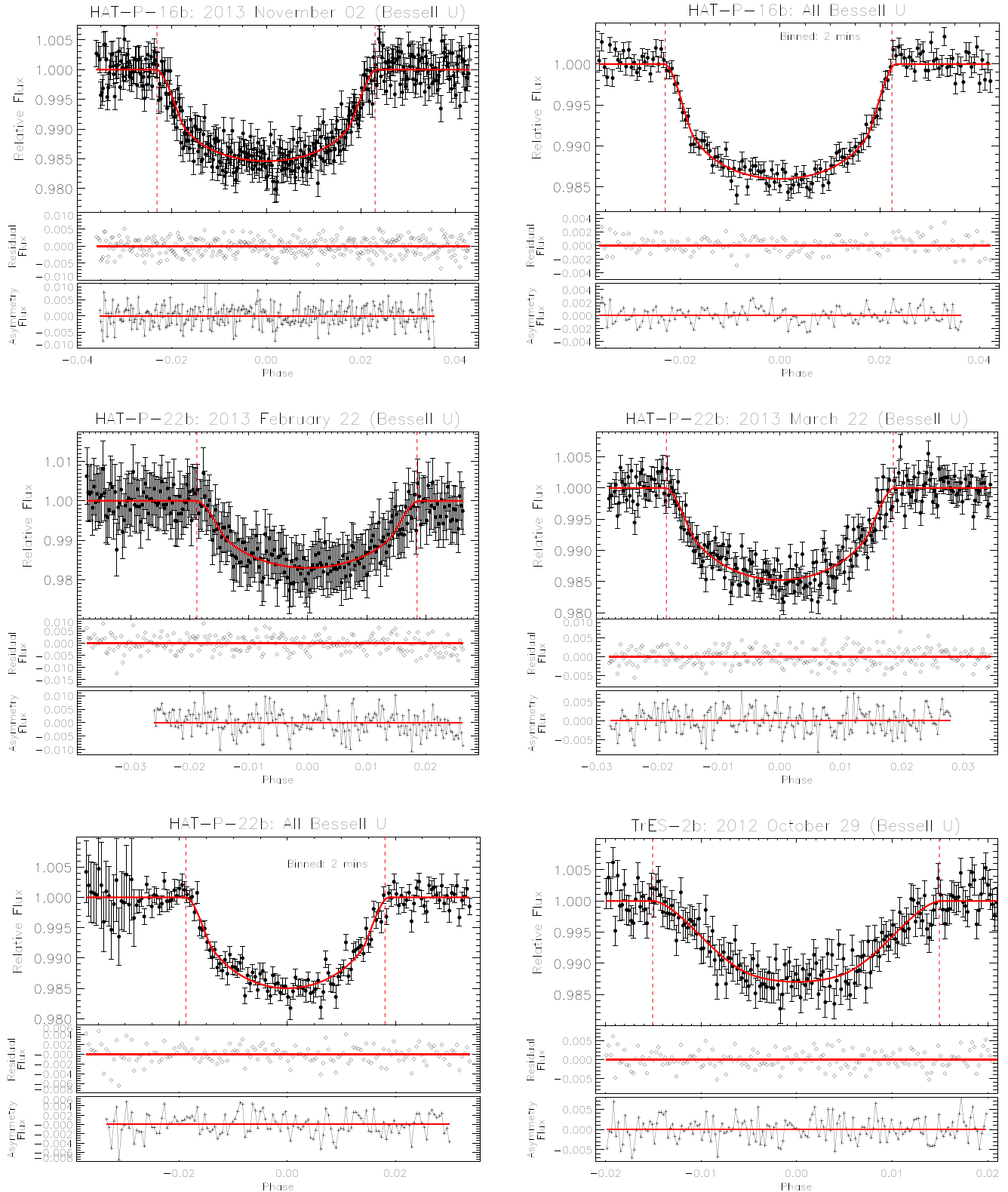


Figure 2. Light curves of HAT-P-16b, HAT-P-22b, and TrES-2b. Other comments are the same as Fig. 1.

The preferred model is the one that produces the lowest BIC value. The BIC has been used extensively in many other exoplanet transit studies (e.g. Gibson et al. 2010, 2013b; Kipping et al. 2010; Croll et al. 2011; Sing et al. 2011; Crossfield et al. 2013; Demory et al.

2013; Howard et al. 2013; Rogers et al. 2013; Murgas et al. 2014; Stevenson et al. 2014a; Zellem et al. 2014).

We perform a Levenberg–Marquardt (LM) non-linear least squares minimization (MPFIT; Press et al. 1992; Markwardt 2009)

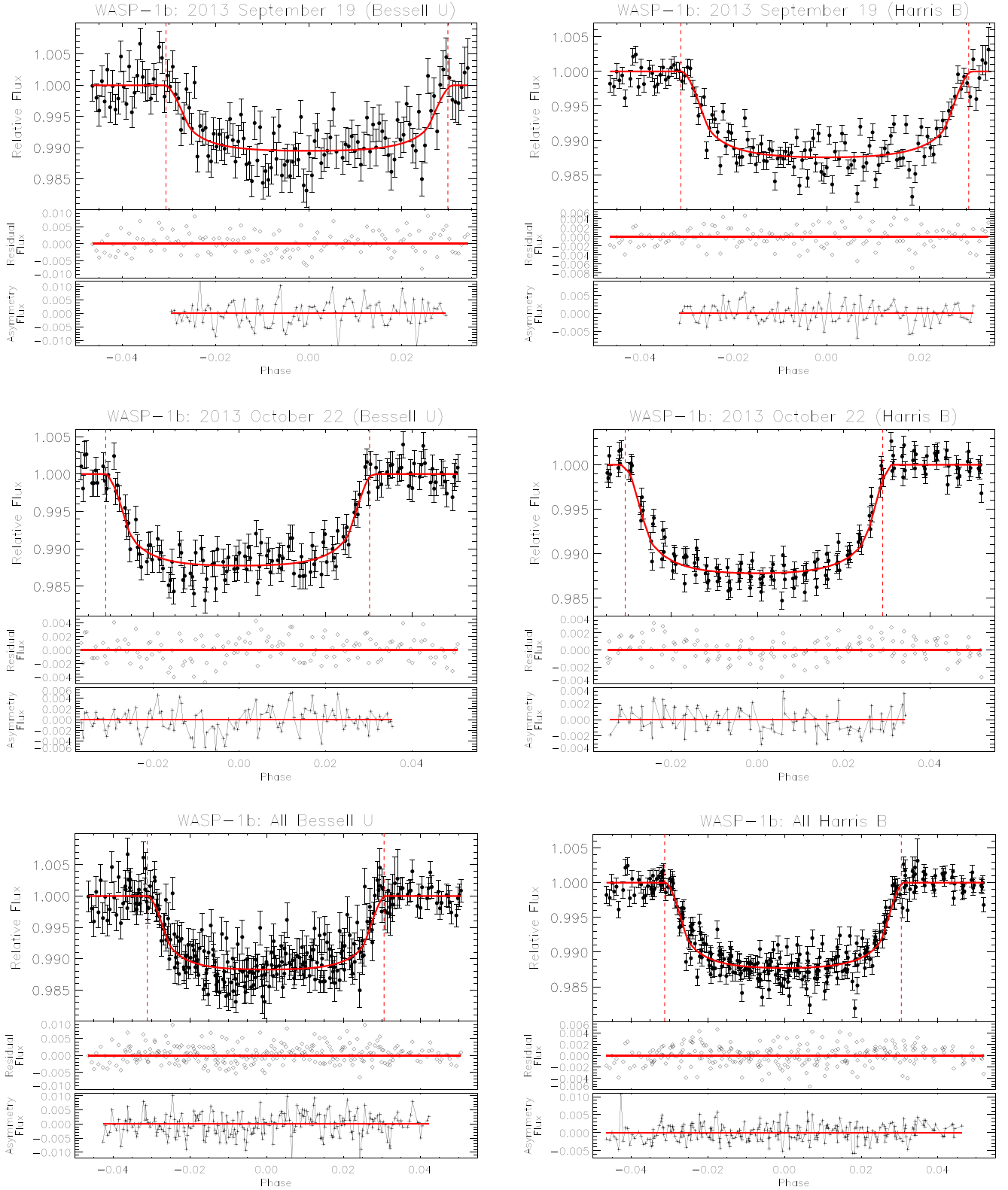


Figure 3. Light curves of WASP-1b. Other comments are the same as Fig. 1.

to find a best fit to the data and a bootstrap Monte Carlo technique (Press et al. 1992) to calculate robust errors of the LM fitted parameters. In addition, we perform a Differential Evolution Markov Chain Monte Carlo (DE-MCMC; Braak 2006; East-

man, Gaudi & Agol 2013) analysis to find a best fit to the data and associated errors. Both the LM and DE-MCMC methods take into account the photometric error bars on the data points.

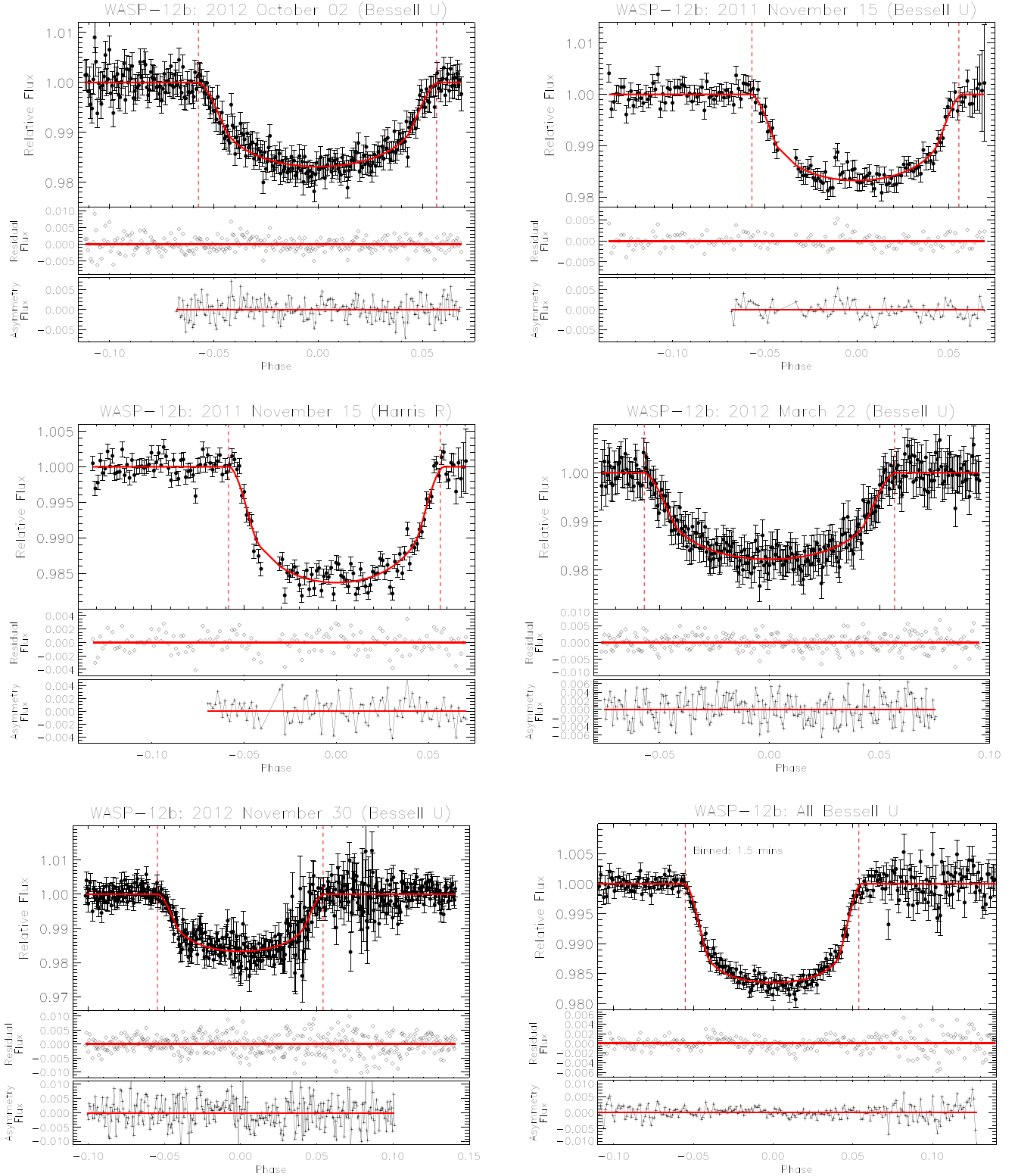


Figure 4. Light curves of WASP-12b. Other comments are the same as Fig. 1.

The formal errors in the LM fit can underestimate the parameter uncertainties under strongly correlated parameters (Popper 1984; Maceroni & Rucinski 1997; Southworth, Maxted & Smalley 2004a,b; Southworth 2008), which is the case for exoplanet transits (Carter & Winn 2009). Therefore, we determine a robust estimation of the uncertainties using the following Monte

Carlo bootstrap procedure. (1) We obtain the best-fitting light curves and parameters from the LM non-linear least squares algorithm. (2) We find new error bars, σ_n , by the following equation

$$\sigma_n = \sigma_p N(\mu, \sigma^2), \quad (3)$$

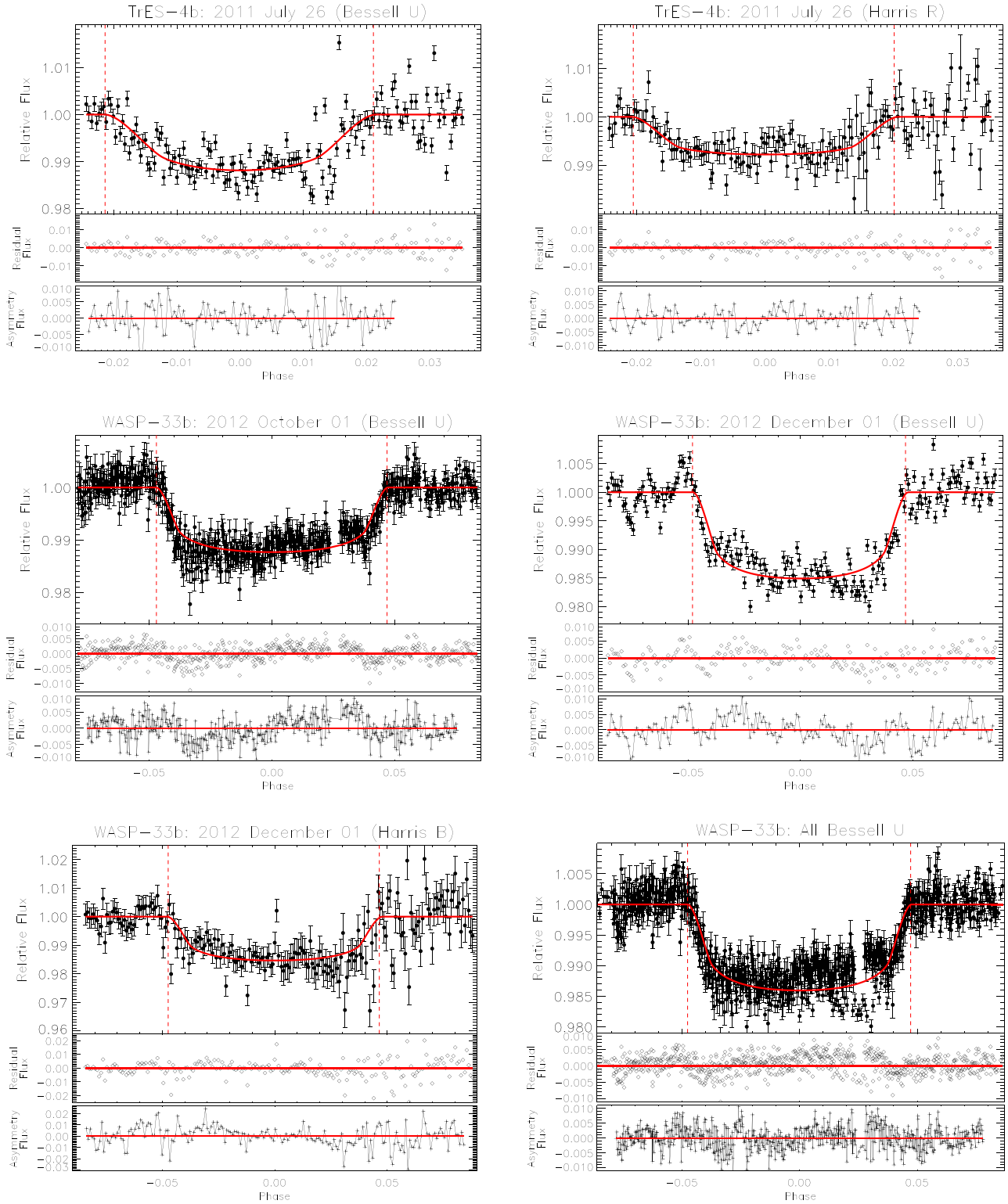


Figure 5. Light curves of TrES-4b and WASP-33b. Other comments are the same as Fig. 1.

where σ_p are the photometric (observational) error bars for each data point in the light curve, $N(\mu, \sigma^2)$ is a random Gaussian distributed variable (N) with a mean $\mu = 0$ and a standard deviation $\sigma = 1$. (3) We add σ_n to the flux measurements in the light curve. (4) Step (1) is repeated to find a new best-fitting light curve (the original photometric error bars, σ_p , are used for the error on the flux measurements). This process is repeated at least 10 000 times to

avoid biasing the Gaussian fit due to small-number statistics. When all iterations are finished, each fit parameter from step (4) is subtracted from the original best-fitting value and a Gaussian function is fit to the distribution. The standard deviations of the distributions are taken as the 1σ uncertainties in the fitted parameters.

We use the DE-MCMC analysis to find more robust parameter values because the solution is a global minimum in solution-space

Table 3. Photometry of all our light curves^a.

Planet name	Filter	Time (BJD _{TDB})	Relative flux	Error bars	CCD X-Pos	CCD Y-Pos	Median Airmass
CoRoT-1b	Bessell- <i>U</i>	2456268.870437	0.995 7161	0.004 7672	549.708	768.763	1.233 0450
CoRoT-1b	Bessell- <i>U</i>	2456268.871252	0.996 1978	0.004 7672	549.505	768.637	1.232 5040
CoRoT-1b	Bessell- <i>U</i>	2456268.872066	0.995 0270	0.004 7406	549.488	768.543	1.231 9960
CoRoT-1b	Bessell- <i>U</i>	2456268.872881	0.992 4044	0.004 6875	548.965	768.693	1.231 5230

^aThis table is available in its entirety in machine-readable form in the online journal. A portion is shown here for guidance regarding its form and content.

and χ^2 . By default, the DE-MCMC in EXOMOP uses 20 chains and 20⁶ links. The Gelman–Rubin statistic (Gelman & Rubin 1992) is used to ensure chain convergence (Ford 2006). We use the DE-MCMC model from EXOFAST (exofast_demc; Eastman et al. 2013) in EXOMOP. EXOMOP uses the Metropolis–Hastings sampler and characterizes the uncertainties using a Bayesian inference that accounts for non-Gaussian errors and covariances between parameters (Eastman et al. 2013). The LM solution and errors are used as the seed for the DE-MCMC model.

EXOMOP is also capable of fitting a function to the OoT baseline to account for any residual curvature due to the atmospheric extinction. Either a linear or quadratic fit can be found in both the LM and DE-MCMC models. The baseline function is fit to the transit simultaneously with the Mandel & Agol (2002) model. The BIC is also used to determine whether to include a baseline fit in the best-fitting model.

3.1.1 Red noise estimation

EXOMOP uses the residual permutation (rosary bead; Southworth 2008), time-averaging (Pont, Zucker & Queloz 2006), and wavelet (Carter & Winn 2009) methods to access the importance of temporally correlated (red) noise in both fitting methods. Red noise is accounted for in our analysis because the errors in the fitted parameter values can be underestimated if we do not account for red noise (Pont et al. 2006; Carter & Winn 2009). In order to be conservative, the red noise method that produces the largest β , the scaling factor of the red noise relative to the white noise errors, is used to inflate the errors in the fitted parameters (Section 3.1.2).

In the residual permutation method (Jenkins, Caldwell & Borucki 2002; Bean et al. 2008; Southworth 2008; Winn et al. 2008b), the best-fitting model is subtracted from the data and the residuals are circularly shifted and then added to the data points. A new fit is found, and then the residuals are shifted again, with those at the end wrapped around to the start of the data. In this way, every new synthetic data set will have the same noise characteristics as the actual data but only translated in time. Usually this process continues until the residuals have cycled back to where they originated (e.g. Todorov et al. 2012). We perform two different residual permutation procedures to determine the effect of red noise in the precision of our derived parameters.

Our first residual permutation (*res1*) method uses a procedure very similar to Todorov et al. (2012) where the shifting process continues until the residuals have cycled back to where they originated (one full circular permutation). The resulting parameter values may have non-Gaussian distributions if red noise is present. Consequently, we set the 1σ error bars of each parameter as half the range that covers 68 per cent of the total number of the data points, centred on the best-fitting value from either the DE-MCMC or LM analysis. For each fitted parameter, we then define β_{res1} (the scaling

factor of the errors relative to white noise using the *res1* method) as $\sigma_w/\sigma_{\text{res1}}$, where σ_w are the error bars derived from the bootstrap Monte Carlo technique or the DE-MCMC technique and the σ_{res1} are the error bars derived from the first residual permutation method.

For the second residual permutation (*res2*) method, we update this procedure by allowing for the error bars of the residuals to be taken into account. This is similar to step (2)–(4) in the bootstrap procedure described above, however, in step (3) σ_n is added to the residuals and in step (4) the residuals are added to the data points and a new fit is found. We repeat this process 10 000 times and on each step the residuals are circularly shifted. This procedure results in a distribution of fitted values for each parameter from which its uncertainty is estimated using the standard deviation of a Gaussian fit. For each fitted parameter, we then define β_{res2} (the scaling factor of the errors relative to white noise using the *res2* method) as $\sigma_w/\sigma_{\text{res2}}$, where σ_{res2} are the error bars derived from the second residual permutation method. The second residual permutation method is limited by the fact that we assume a Gaussian distribution for the errors.

The next red noise estimation we implement is the time-averaging method. This is done in a similar fashion to the procedure described by Winn et al. (2008b). For each light curve, we find the best-fitting model and calculate the residuals between the observed and calculated fluxes. Next, the residuals are separated into bins of N points and we calculate the standard deviation, σ_N , of the binned residuals. In our analysis, N ranges from 1 to n , where n is the total number of data points in each respective transit. Using the set of σ_N and N values, we then use an LM non-linear least squares minimization algorithm to find the rms of red noise (σ_{red}) and the rms of white noise (σ_{white}) using the following equation from Pont et al. (2006):

$$\sigma_N = \sqrt{\frac{\sigma_{\text{white}}^2}{N} + \sigma_{\text{red}}^2}. \quad (4)$$

Using σ_{white} and σ_{red} we estimate β_{time} , the scaling factor of the errors relative to white noise using the time-averaging method, with the following equation from Carter & Winn (2009):

$$\beta_{\text{time}} = \sqrt{1 + \left(\frac{\sigma_{\text{red}}}{\sigma_{\text{white}}}\right)^2}. \quad (5)$$

Finally, we use the wavelet technique (solverdwv; Carter & Winn 2009) as a third check of the importance of red noise in the light-curve fitting process. In this method, the total noise of the transit is assumed to be formed as an additive combination of noise with power spectral density proportional to $1/f^\alpha$ (the red noise) and Gaussian white noise. A downhill simplex method (AMOEBA; Nelder & Mead 1965; Press et al. 1992) algorithm is used to maximize the likelihood that a function of σ_{red} and σ_{white} is related to the standard deviations of the $1/f^\alpha$ and white noise, respectively. A

more thorough description of the wavelet model can be found in Carter & Winn (2009). Again, β_{wave} , the scaling factor of the errors relative to white noise using the wavelet technique, is estimated by using equation (5).

3.1.2 Final error bars on the fitted parameters

To get the final error bars for the fitted parameters, we multiply σ_w by the largest β (β_{time} , β_{res1} , β_{res2} , or β_{wave}) from the residual permutation, time-averaging, and wavelet red noise calculations to account for underestimated error bars due to red noise (Winn et al. 2008b). To remain conservative, this multiplication step is only done if the largest β is greater than one. Finally, in cases where the reduced chi-squared (χ_r^2) of the data (Table 2) to the best-fitting model is greater than unity we multiply the error bars above by $\sqrt{\chi_r^2}$ to compensate for the underestimated observational errors (Bruntt et al. 2006; Southworth, Wheatley & Sams 2007a; Southworth et al. 2007b; Southworth 2008; Barnes et al. 2013).

3.1.3 Additional features of EXOMOP

We calculate the transit duration, τ_t , of each of our transit model fits with the following equation (Carter et al. 2008):

$$\tau_t = t_{\text{egress}} - t_{\text{ingress}}, \quad (6)$$

where t_{egress} is the best-fitting model time of egress (fourth contact), and t_{ingress} is the best-fitting model time of ingress (first contact). The error on τ_t is set to the $\sqrt{2}$ times the cadence of our observations (Carter & Winn 2009).

EXOMOP performs an asymmetry test on each transit. We subtract each light curve by the mirror image of itself about the calculated mid-transit time. This same technique is used in Turner et al. (2013) and Pearson et al. (2014) to search for asymmetries caused by a possible bow shock in TrES-3b and HAT-P-16b, respectively. This technique is useful for possible bow shock detection because bow shock models of WASP-12b (Llama et al. 2011) and HD 189733b (Llama et al. 2013) predict a distinct asymmetry between the two halves of the transit (Llama et al. 2011, see fig. 2; Llama et al. 2013, see fig. 3).

3.2 EXOMOP MODEL COMPARISON

Using artificial data, we perform several different comparison tests of EXOMOP with two different publicly available modelling software packages: the Transit Analysis Package⁶ (TAP; Mandel & Agol 2002; Carter & Winn 2009; Gazak et al. 2012; Eastman et al. 2013) and JKTEBOP⁷ (Southworth et al. 2004a,b). We also test if the errors we calculate using EXOMOP are reliable by comparing the errors to analytic estimates.

We briefly discuss these two modelling packages below. TAP fits the transit light curves with a standard Mandel & Agol (2002) model using MCMC techniques and the parameter uncertainties are found with a wavelet likelihood function (Carter & Winn 2009). JKTEBOP was adapted from the EBOP program written for eclipsing binary star systems (Popper & Etzel 1981) and implements the Nelson–Davis–Etzel eclipsing binary model (Nelson & Davis 1972). JKTEBOP and

TAP both implement spherical models. In addition, JKTEBOP uses a Monte Carlo simulation algorithm to compute errors (Southworth et al. 2004a,b; Southworth 2010; Hoyer et al. 2011).

We create a synthetic model transit using the analytic equations of Mandel & Agol (2002) with a planet-to-star radius (R_p/R_*) = 0.1173, the scaled semimajor axis (a/R_*) = 3.033, inclination (i) = 82°96, period (P_p) = 1.091 4209 d, the linear limb darkening coefficient (μ_1) = 0.617 972 03, the quadratic limb darkening coefficient (μ_2) = 0.208 134 38, eccentricity (e) = 0, and argument of periastron (ω) = 0°. These parameters are chosen because they match the parameters of WASP-12b observed in the near-UV. Next, three sets of different white and red noise parameters are added to the synthetic Mandel & Agol (2002) model to explore the effects of noise. The first set of models include only random Gaussian white noise with a standard deviation of 1, 2, 4, and 5 mmag. For the second and third set, we create white noise and $1/f^{\alpha}$ red noise both with a standard deviation of 1 mmag where α is equal to 0.33 and 0.66, respectively. In total, we ran six models.

For the EXOMOP analysis, we use 10 000 iterations for the LM fit and 20 chains and 20^6 links for the DE-MCMC fit. With TAP, we model each transit individually using five chains with lengths of 10^5 links each. JKTEBOP is implemented using the Monte Carlo algorithm and residual permutation method described in Southworth (2008). During the analysis for each model, the time of mid-transit (T_c) and R_p/R_* are allowed to float. We only model these two parameters for the comparison tests because the errors on them are analytically tractable (see below; Carter et al. 2008). The i , e , ω , μ_1 , μ_2 , a/R_* , and the P_p of the planet are fixed. In addition, for TAP the white and red noise are left as free parameters. Since TAP does not automatically ensure chain convergence, we perform the Gelman–Rubin statistic (Gelman & Rubin 1992; Ford 2006) manually to ensure convergence. In addition, TAP does not take into account the individual error bars on each transit point, whereas both the EXOMOP and JKTEBOP models do take them into account.

The results of the white noise analysis can be found in Table 4 and the red noise analysis in Table 5. As expected, EXOMOP finds no red noise in the pure white noise tests and red noise in the red noise tests. In every case, the EXOMOP R_p/R_* values are within 1σ to the true R_p/R_* . We find that TAP overestimates the amount of red noise in every test we ran (by 2σ – 14σ) including the set of models with only white noise. Consequently, TAP is overestimating the error bars to their fitted parameters because of this excess red noise. Since both EXOMOP and TAP use the wavelet likelihood technique (Carter & Winn 2009), it is not clear why TAP is overestimating the amount of red noise in these tests. Our results confirm the need to account for red noise using a variety of methods. Each of the methods used find red noise in the red noise tests but at slightly varying degrees. Turner et al. (2013) and Hoyer, Rojo & López-Morales (2012) both conclude that JKTEBOP may be underestimating the errors in its transit fits when compared to TAP. However, neither of these studies conduct a thorough red and white noise test study. Therefore, we believe that TAP is overestimating the error bars in the fitted parameters compared to JKTEBOP and EXOMOP due to its incorrect red noise calculation. The EXOMOP and JKTEBOP results are in very good agreement with each other.

To get a general idea if the error estimation in EXOMOP is behaving as expected, we compare our white noise tests (Table 4) to analytic estimations for the uncertainty in the flux drop, $\delta = (R_p/R_*)^2$, and mid-transit time. Carter et al. (2008) derive an analytic estimate for the 1σ uncertainty in δ (σ_δ) to be

$$\sigma_\delta = \frac{\sigma_\delta}{\sqrt{n}}, \quad (7)$$

⁶ <http://ifa.hawaii.edu/users/zgazak/IfA/TAP.html>

⁷ <http://www.astro.keele.ac.uk/jkt/codes/jktebop.html>

Table 4. White Gaussian noise model tests with EXOMOP, TAP, and JKTEBOP using synthetic light curves.

Model	Noise (mmag)	R_p/R_*	Mid-transit (HJD)	Red ^a (mmag)	White ^a (mmag)	$\beta_{\text{res}2}$ R_p/R_*	$\beta_{\text{res}1}$ R_p/R_*	$\beta_{\text{res}2}$ Mid	$\beta_{\text{res}1}$ Mid	Red ^b (mmag)	White ^b (mmag)
TAP	1	$0.11785^{+0.00065}_{-0.00068}$	$0.00000^{+0.00024}_{-0.00024}$	$2.8^{+1.7}_{-1.6}$	$0.94^{+0.03}_{-0.03}$	—	—	—	—	—	—
TAP	2	$0.1168^{+0.0012}_{-0.0012}$	$-0.00027^{+0.00045}_{-0.00044}$	$3.8^{+3.1}_{-2.5}$	$1.96^{+0.07}_{-0.06}$	—	—	—	—	—	—
TAP	4	$0.1170^{+0.0027}_{-0.0027}$	$-0.0007^{+0.0010}_{-0.0010}$	$11.4^{+7.0}_{-6.6}$	$3.79^{+0.13}_{-0.13}$	—	—	—	—	—	—
TAP	5	$0.1165^{+0.0036}_{-0.0034}$	$-0.0007^{+0.0012}_{-0.0012}$	$14.6^{+9.9}_{-8.8}$	$5.06^{+1.18}_{-0.18}$	—	—	—	—	—	—
JKTEBOP	1	$0.11775^{+0.00025}_{-0.00025}$	$0.00003^{+0.00013}_{-0.00013}$	—	—	—	1.78	—	0.99	—	—
JKTEBOP	2	$0.11743^{+0.00052}_{-0.00052}$	$-0.00032^{+0.00028}_{-0.00028}$	—	—	—	0.79	—	0.88	—	—
JKTEBOP	4	$0.1174^{+0.0010}_{-0.0010}$	$-0.00070^{+0.00053}_{-0.00053}$	—	—	—	0.31	—	0.80	—	—
JKTEBOP	5	$0.1160^{+0.0013}_{-0.0013}$	$-0.00056^{+0.00069}_{-0.00069}$	—	—	—	0.54	—	0.79	—	—
EXOMOP	1	$0.11769^{+0.00025}_{-0.00025}$	$0.00001^{+0.00013}_{-0.00013}$	0.0	0.94	0.97	0.58	0.96	0.85	0.00	$0.93^{+0.33}_{-0.33}$
EXOMOP	2	$0.11738^{+0.00051}_{-0.00050}$	$-0.00031^{+0.00028}_{-0.00028}$	0.0	1.84	0.45	0.90	0.84	0.88	0.00	$1.75^{+0.70}_{-0.70}$
EXOMOP	4	$0.1173^{+0.0011}_{-0.0011}$	$-0.00067^{+0.00059}_{-0.00057}$	0.0	3.84	0.91	0.72	0.93	0.74	0.00	$3.44^{+1.60}_{-1.60}$
EXOMOP	5	$0.1159^{+0.0013}_{-0.0013}$	$-0.00057^{+0.00062}_{-0.00062}$	0.0	5.12	0.89	0.65	0.89	0.76	0.00	$4.80^{+2.22}_{-2.22}$

^aThe red and white noise are calculated using the wavelet likelihood technique (Carter & Winn 2009) described in Section 3.1.1.^bThe red and white noise are calculated using the time-averaging method (Pont et al. 2006) described in Section 3.1.1.**Table 5.** Red noise model tests with EXOMOP, TAP, and JKTEBOP using synthetic light curves.

Model	α Added	R_p/R_*	Mid-transit (HJD)	Red ^a (mmag)	White ^a (mmag)	$\beta_{\text{res}2}$ R_p/R_*	$\beta_{\text{res}1}$ R_p/R_*	$\beta_{\text{res}2}$ Mid	$\beta_{\text{res}1}$ Mid	Red ^b (mmag)	White ^b (mmag)
TAP	0.66	$0.1197^{+0.0022}_{-0.0023}$	$-0.00045^{+0.00061}_{-0.00062}$	$13.2^{+1.4}_{-1.4}$	$0.618^{+0.053}_{-0.059}$	—	—	—	—	—	—
TAP	0.33	$0.1176^{+0.0016}_{-0.0016}$	$-0.00054^{+0.00046}_{-0.00047}$	$9.1^{+1.5}_{-1.4}$	$0.856^{+0.043}_{-0.043}$	—	—	—	—	—	—
JKTEBOP	0.66	$0.11889^{+0.00067}_{-0.00067}$	$-0.000036^{+0.00028}_{-0.00028}$	—	—	2.59	—	—	2.18	—	—
JKTEBOP	0.33	$0.11693^{+0.00052}_{-0.00052}$	$-0.00038^{+0.00022}_{-0.00022}$	—	—	1.99	—	—	1.61	—	—
EXOMOP	0.66	$0.1177^{+0.0015}_{-0.0029}$	$-0.00004^{+0.00029}_{-0.00029}$	0.46	0.70	1.41	4.53	1.43	3.61	$0.55^{+0.19}_{-0.19}$	$1.41^{+0.65}_{-0.65}$
EXOMOP	0.33	$0.11817^{+0.00081}_{-0.00081}$	$-0.00018^{+0.00040}_{-0.00059}$	0.16	0.91	1.44	1.67	1.42	1.74	$0.07^{+0.34}_{-0.07}$	$1.53^{+0.46}_{-0.46}$

^aThe red and white noise are calculated using the wavelet likelihood technique (Carter & Winn 2009) described in Section 3.1.1.^bThe red and white noise are calculated using the time-averaging method (Pont et al. 2006) described in Section 3.1.1.

where σ_g are the Gaussian errors in the relative flux (in our case the noise added) and n is the number of data points. Additionally, the analytic estimate of the 1σ uncertainty (σ_t) in the mid-transit time is (Carter et al. 2008)

$$\sigma_t = \frac{\sigma_g}{\sqrt{n\delta}} (\tau_t - \tau) \sqrt{\frac{\tau}{2(\tau_t - \tau)}}, \quad (8)$$

where τ is the ingress/egress duration. Limb darkening and red noise cause the error estimation in equations (7) and (8) to increase (Seager 2011). The error estimations we find using EXOMOP have the same behaviour as the analytic estimates by Carter et al. (2008) exactly for both σ_δ and σ_t . For example, if the noise doubles in our white noise tests then the error estimates on R_p/R_* also double (Table 4). The JKTEBOP error bars also mimic this analytic behaviour but the TAP error bars do not. Due to this result, we believe the error estimation in EXOMOP is reliable.

3.3 EXOMOP ANALYSIS OF THE SYSTEMS

Each individual transit is modelled with EXOMOP using 10 000 iterations for the LM model and 20 chains and 20^6 links for the DE-MCMC model. During the analysis T_c and R_p/R_* are always left as free parameters for each transit. We then systematically fit every combination with a/R_* , i , T_c , and R_p/R_* set as free parameters. The BIC is used to assess overfitting of the data and the model that

produces the lowest BIC value is always chosen. For every planet except HAT-P-13b, WASP-12b, WASP-44b, and WASP-77Ab the BIC is higher when fitting for a/R_* and i . The a/R_* , e , ω , i , and P_p of each of the planets are fixed to their values listed in Table 6. The linear and quadratic limb darkening coefficients in each filter are taken from Claret & Bloemen (2011) and interpolated to the stellar parameters of the host stars (see Table 7) using the EXOFAST applet⁸ (Eastman et al. 2013). In addition, a linear or quadratic least squares fit is modelled to the OoT baseline simultaneously with the Mandel & Agol (2002) model. The BIC is also used to determine whether to include a linear or quadratic OoT baseline fit in the best-fitting model.

The fitted parameters from either the LM or DE-MCMC best-fitting model that produce the highest error bars are reported. In every case, both models find results within 1σ of each other. The light-curve parameters obtained from the EXOMOP analysis and the derived transit durations are summarized in Tables 8–12. The modelled light curves can be found in Figs 1–7. The physical parameters for our targets are derived as outlined in Section 4 (Tables 13 and 14). A thorough description of the modelling and results of each system can be found in Section 5. We also perform the asymmetry

⁸ <http://astroutils.astronomy.ohio-state.edu/exofast/limbdark.shtml>

Table 6. Parameters fixed for the light-curve fitting using EXOMOP. References. – (1) Gillon et al. (2009); (2) Knutson et al. (2014); (3) Nikolov et al. (2014); (4) Southworth et al. (2012a); (5) Pearson et al. (2014); (6) Bakos et al. (2011); (7) Esteves, De Mooij & Jayawardhana (2013); (8) Chan et al. (2011); (9) Maciejewski et al. (2014); (10) Sing et al. (2013); (11) Kovács et al. (2013); (12) Smith et al. (2012); (13) Mancini et al. (2013); (14) Enoch et al. (2011); (15) Maxted et al. (2013).

Planet	Period (d)	a/R_*	Inclination (°)	Eccentricity	Omega (°)	Source
CoRoT-1b	1.508 9686	5.259	85.66	0.071	276.70	1
GJ436b	2.643 8986	14.41	86.774	0.15	351	2
HAT-P-1b	4.465 29976	9.853	85.634	0.00	0.00	3
HAT-P-13b	2.916 2383	–	81.93	0.00	0.00	4
HAT-P-16b	2.775 9690	7.17	86.6	0.034	214	5
HAT-P-22b	3.212 220	8.55	86.90	0.016	156.00	6
TrES-2b	2.470 6132	7.8957	83.8646	0.0002	143.13	7
TrES-4b	3.553 9268	6.08	82.81	0.00	0.00	8
WASP-1b	2.519 9449	5.64	88.65	0.00	0.00	9
WASP-12b	1.091 42166	–	82.72	0.0447	274.44	10
WASP-33b	1.219 8709	3.69	86.2	0.00	0.00	11
WASP-36b	1.537 3653	5.977	83.61	0.00	0.00	12
WASP-44b	2.423 8133	8.562	86.59	0.00	0.00	13
WASP-48b	2.143 634	4.23	80.09	0.00	0.00	14
WASP-77Ab	1.360 0309	–	89.4	0.00	0.00	15

Table 7. Limb darkening coefficients for the light-curve fitting using EXOMOP. References. – (a) Barge et al. (2008); (b) Moses et al. (2013); (c) Bean, Benedict & Endl (2006); (d) Torres, Winn & Holman (2008); (e) Torres et al. (2008); (f) Bakos et al. (2009); (g) Buchhave et al. (2010); (h) Bakos et al. (2011); (i) Torres et al. (2008); (j) Torres et al. (2008); (k) Simpson et al. (2011); (l) Hebb et al. (2009); (m) Collier Cameron et al. (2010); (n) Smith et al. (2012); (o) Anderson et al. (2012); (p) Enoch et al. (2011); (q) Maxted et al. (2013).

Planet	Filter	Linear coefficient ^a	Quadratic coefficient ^a	T_{eff} (K)	(Fe/H)	$\log g$ (cgs)
CoRoT-1b(a)	Bessell <i>U</i>	0.665 47	0.173 02	5950	– 0.30	4.25
GJ436b	Bessell <i>U</i>	0.926 888	– 0.120 646	3350(b)	– 0.15(c)	4.427(d)
HAT-P-1b(e)	Bessell <i>U</i>	0.734 17	0.112 38	5980	+0.130	4.382
HAT-P-13b(f)	Bessell <i>U</i>	0.892 73	– 0.029 40	5653	+0.410	4.130
HAT-P-16b(g)	Bessell <i>U</i>	0.657 20	0.176 53	6158	+0.170	4.340
HAT-P-22b(h)	Bessell <i>U</i>	1.003 92	– 0.143 38	5302	+0.24	4.36
TrES-2b(i)	Bessell <i>U</i>	0.747 42	0.102 32	5850	– 0.15	4.427
TrES-4b(j)	Bessell <i>U</i>	0.618 10	0.209 52	6200	0.140	4.064
WASP-1b	Bessell <i>U</i>	0.151 543	0.687 788	6110(k)	0.26(d)	4.190(d)
”	Harris <i>B</i>	0.198 846	0.599 307	6110	0.26	4.190
WASP-12b(l)	Harris <i>R</i>	0.617 97	0.208 13	6300	0.30	4.38
”	Bessell <i>U</i>	0.300 70	0.319 83	6300	0.30	4.38
WASP-33b(m)	Bessell <i>U</i>	0.316 68	0.386 43	7430	+0.10	4.30
”	Harris <i>B</i>	0.371 46	0.351 68	7430	+0.10	4.30
WASP-36b(n)	Harris <i>R</i>	0.321 06	0.301 31	5880	– 0.31	4.498
”	Bessell <i>U</i>	0.705 03	0.139 79	5880	– 0.31	4.498
WASP-44b(o)	Bessell <i>U</i>	0.939 16	– 0.065 61	5410	+0.06	4.481
”	Harris <i>V</i>	0.550 120	0.199 928	5410	+0.06	4.481
”	Harris <i>B</i>	0.758 312	0.072 8504	5410	+0.06	4.481
WASP-48b(p)	Bessell <i>U</i>	0.702 17	0.141 81	5920	– 0.12	4.03
WASP-77Ab(q)	Bessell <i>U</i>	0.926 96	– 0.062 41	5500	0.00	4.33

^aThe limb darkening coefficients are taken from Claret & Bloemen (2011) and interpolated to the stellar parameters of their host star.

test (described in Section 3.1.3) for each transit to search for any non-spherical asymmetries.

4 CALCULATED PHYSICAL PROPERTIES OF THE SYSTEMS

We use the results of our light-curve modelling with EXOMOP to calculate the planetary and geometrical parameters of our targets (mass,

radius, density, surface gravity, equilibrium temperature, Safronov number, atmospheric scaleheight). The physical parameters of all our systems can be found in Tables 13 and 14. The planetary mass, M_p , can be calculated using the following equation (Winn 2010; Seager 2011):

$$M_p = \left(\frac{\sqrt{1-e^2}}{28.4329} \right) \left(\frac{K_*}{\sin i} \right) \left(\frac{P_b}{\text{yr}} \right)^{1/3} \left(\frac{M_*}{M_\odot} \right)^{2/3} M_{\text{jup}}, \quad (9)$$

Table 8. Parameters derived in this study for the CoRoT-1b, GJ436b, HAT-P-1b, HAT-P-16b, HAT-P-22b, TrES-2b, TrES-4b, and WASP-1b light curves using EXOMOP.

Planet	CoRoT-1b	GJ436b	GJ436b	GJ436b	HAT-P-1b
Date	2012 December 06	2012 March 23	2012 April 07	All	2012 October 02
Filter ^a	<i>U</i>	<i>U</i>	<i>U</i>	<i>U</i>	<i>U</i>
T_c (HJD-2450000)	6268.989 63 ^{+0.000 70} _{-0.0013}	6009.8889 ^{+0.0019} _{-0.0020}	6025.7322 ^{+0.0073} _{-0.0068}	–	6203.649 07 ^{+0.000 84} _{-0.000 95}
R_p/R_*	0.1439 ^{+0.0020} _{-0.0018}	0.0930 ^{+0.0083} _{-0.0048}	0.0703 ^{+0.0099} _{-0.0071}	0.0758 ^{+0.0086} _{-0.0075}	0.1189 ^{+0.0010} _{-0.0014}
Duration (min)	149.9 ^{+1.9} _{-1.9}	59.6 ^{+2.5} _{-2.5}	58.30 ^{+1.45} _{-1.45}	59.55 ^{+1.07} _{-1.07}	172.12 ^{+0.95} _{-0.95}
$\beta_{\text{res}2}^b$ (R_p/R_*)	0.74	0.79	1.17	1.14	1.35
$\beta_{\text{res}2}^b$ (Mid)	0.74	0.75	1.15	–	1.30
$\beta_{\text{res}1}^c$ (R_p/R_*)	+1.04 – 0.70	+1.92 – 0.59	+2.35 – 1.67	+2.64 – 2.28	+1.33 – 1.94
$\beta_{\text{res}1}^c$ (Mid)	+0.70 – 2.02	+1.16 – 1.48	+2.15 – 2.00	–	+2.13 – 2.43
β_{time}^d	1.00	1.00	1.03	1.01	1.03
White noise ^e (mmag)	2.47 ^{+1.04} _{-1.04}	1.87 ^{+0.66} _{-0.66}	2.52 ^{+1.41} _{-1.41}	2.86 ^{+1.38} _{-1.38}	1.50 ^{+0.64} _{-0.64}
Red noise ^e (mmag)	0.00	0.00	0.66 ^{+1.05} _{-0.66}	0.40 ^{+0.75} _{-0.40}	0.35 ^{+0.29} _{-0.29}
β_{wavelet}^f	1.01	1.004	1.03	1.01	1.02
White noise ^g (mmag)	3.47	2.19	2.08	1.95	1.28
Red noise ^g (mmag)	0.00	0.20	0.49	0.32	0.25
OoT baseline function	None	None	None	–	None
Planet	HAT-P-16b	HAT-P-16b	HAT-P-22b	HAT-P-22b	HAT-P-22b
Date	2013 November 02	All	2013 February 22	2013 March 22	All
Filter ^a	<i>U</i>	<i>U</i>	<i>U</i>	<i>U</i>	<i>U</i>
T_c (HJD-2450000)	6598.791 10 ^{+0.000 60} _{-0.000 59}	–	6346.8144 ^{+0.0013} _{-0.0014}	6738.708 64 ^{+0.000 61} _{-0.000 63}	–
R_p/R_*	0.1115 ^{+0.0011} _{-0.0011}	0.106 45 ^{+0.000 67} _{-0.000 67}	0.1151 ^{+0.0021} _{-0.0022}	0.1072 ^{+0.0013} _{-0.0012}	0.107 97 ^{+0.000 86} _{-0.000 94}
Duration (min)	185.44 ^{+1.28} _{-1.28}	181.78 ^{+3.06} _{-3.06}	172.46 ^{+1.66} _{-1.66}	172.89 ^{+2.38} _{-2.38}	170.50 ^{+3.05} _{-3.05}
$\beta_{\text{res}2}^b$ (R_p/R_*)	0.67	1.08	0.50	0.71	1.18
$\beta_{\text{res}2}^b$ (Mid)	0.88	–	0.51	0.83	–
$\beta_{\text{res}1}^c$ (R_p/R_*)	+0.16 – 0.24	+0.29 – 0.38	0.10–0.70	0.23–0.15	0.53–0.56
$\beta_{\text{res}1}^c$ (Mid)	+0.75 – 0.54	–	0.59–0.53	0.53–0.32	–
β_{time}^d	1.00	1.00	1.00	1.00	1.00
White noise ^e (mmag)	1.23 ^{+0.61} _{-0.61}	0.97 ^{+0.25} _{-0.25}	2.23 ^{+0.65} _{-0.65}	1.11 ^{+0.52} _{-0.52}	1.19 ^{+0.36} _{-0.36}
Red noise ^e (mmag)	0.00	0.00	0.00	0.00	0.00
β_{wavelet}^f	1.00	1.00	1.00	1.00	1.00
White noise ^g (mmag)	2.07	0.86	3.06	2.07	1.42
Red noise ^g (mmag)	0.00	0.00	0.20	0.00	0.00
OoT baseline function	Linear	–	None	Linear	–
Planet	TrES-2b	TrES-4	TrES-4b	WASP-1b	WASP-1b
Date	2012 October 29	2011 July 26	2011 July 26	2013 September 19	2013 September 19
Filter ^a	<i>U</i>	<i>R</i>	<i>U</i>	<i>U</i>	<i>B</i>
T_c (HJD-2450000)	6230.5980 ^{+0.000 59} _{-0.000 60}	5769.7536 ^{+0.0040} _{-0.0040}	5769.7532 ^{+0.0036} _{-0.0037}	6555.9381 ^{+0.0038} _{-0.0025}	6555.9393 ^{+0.0027} _{-0.0027}
R_p/R_*	0.1243 ^{+0.0022} _{-0.0024}	0.0880 ^{+0.0055} _{-0.0055}	0.1094 ^{+0.0052} _{-0.0052}	0.0938 ^{+0.0023} _{-0.0023}	0.1018 ^{+0.0040} _{-0.0040}
Duration (min)	106.68 ^{+1.19} _{-1.19}	205.35 ^{+2.73} _{-2.73}	216.96 ^{+2.64} _{-2.64}	219.49 ^{+3.15} _{-3.15}	224.17 ^{+3.18} _{-3.18}
$\beta_{\text{res}2}^b$ (R_p/R_*)	0.72	1.6	2.23	1.28	1.89
$\beta_{\text{res}2}^b$ (Mid)	0.97	1.46	2.25	1.19	1.68
$\beta_{\text{res}1}^c$ (R_p/R_*)	+0.26 – 0.27	+0.54 – 0.85	+0.67 – 0.74	+0.43 – 0.58	+0.45 – 0.67
$\beta_{\text{res}1}^c$ (Mid)	+0.32 – 0.86	+1.30 – 1.24	+1.14 – 1.15	+1.96 – 1.28	+1.03 – 1.10
β_{time}^d	1.00	1.00	1.00	1.01	1.00
White noise ^e (mmag)	1.67 ^{+0.53} _{-0.53}	1.78 ^{+1.05} _{-1.05}	3.79 ^{+1.40} _{-1.40}	3.12 ^{+1.76} _{-1.76}	2.09 ^{+0.90} _{-0.90}
Red noise ^e (mmag)	0.00	0.00	0.00	0.32 ^{+0.32} _{-0.32}	0.00
β_{wavelet}^f	1.00	1.00	1.00	1.00	1.00
White noise ^g (mmag)	2.23	3.08	3.32	2.37	1.69
Red noise ^g (mmag)	0.00	0.001	0.001	0.00	0.00
OoT baseline function	Linear	Quad	Linear	Linear	Linear

^aFilter: *B* is the Harris *B* (330–550 nm), *R* is the Harris *R* (550–900 nm), *V* is the Harris *V* (473–686 nm) and *U* is the Bessell *U* (303–417 nm).^b $\beta_{\text{res}2}$ is found by using the second residual permeation method (Section 3.1.1).^c $\beta_{\text{res}1}$ is found by using the first residual permeation method (Section 3.1.1).^d β_{time} is the scaling factor for the time-averaging method (Pont et al. 2006, Section 3.1.1).^eThe red and white noise are calculated using the time-averaging method (Pont et al. 2006, Section 3.1.1).^f β_{wave} is the scaling factor for the wavelet likelihood technique (Carter & Winn 2009, Section 3.1.1).^gThe red and white noise are calculated using the wavelet likelihood technique (Carter & Winn 2009, Section 3.1.1).

Table 9. Parameters derived in this study for the WASP-1b, WASP-33b, WASP-36b, and WASP-44b light curves using EXOMOP.

Planet	WASP-1b	WASP-1b	WASP-1b	WASP-1b	WASP-33b
Date	2013 October 22	2013 October 22	All	All	2012 December 01
Filter ^a	<i>U</i>	<i>B</i>	<i>U</i>	<i>B</i>	<i>U</i>
T_c (HJD-2450000)	6588.69 666 ^{+0.000 90} _{-0.000 82}	6588.6961 ^{+0.0008} _{-0.0012}	—	—	6263.8434 ^{+0.0022} _{-0.0029}
R_p/R_*	0.096 30 ^{+0.000 92} _{-0.000 92}	0.100 96 ^{+0.000 97} _{-0.000 97}	0.0964 ^{+0.0010} _{-0.0010}	0.1013 ^{+0.0018} _{-0.0018}	0.1125 ^{+0.0047} _{-0.0097}
Duration (min)	222.01 ^{+3.22} _{-3.22}	213.71 ^{+3.22} _{-3.22}	223 ^{+1.83} _{-1.83}	224.17 ^{+1.83} _{-1.83}	164.77 ^{+2.15} _{-2.15}
$\beta_{\text{res}2}^b$ (R_p/R_*)	1.03	1.26	1.41	1.73	2.81
$\beta_{\text{res}2}^b$ (Mid)	1.00	1.20	—	—	2.70
$\beta_{\text{res}1}^c$ (R_p/R_*)	+0.69 −0.81	+0.81 −0.30	+0.64 −0.57	+1.63 −0.73	+3.88 −8.40
$\beta_{\text{res}1}^c$ (Mid)	+1.53 −1.40	+1.50 −2.20	—	—	+3.60 −4.55
β_{time}^d	1.03	1.06	1.002	1.01	1.10
White noise ^e (mmag)	1.71 ^{+0.96} _{-0.96}	1.12 ^{+0.70} _{-0.70}	1.28 ^{+0.72} _{-0.72}	1.81 ^{+0.94} _{-0.94}	2.73 ^{+1.31} _{-1.31}
Red noise ^e (mmag)	0.39 ^{+0.62} _{-0.39}	0.41 ^{+0.30} _{-0.30}	0.17 ^{+0.90} _{-0.17}	0.29 ^{+0.33} _{-0.29}	1.23 ^{+2.82} _{-1.23}
β_{wave}^f	1.00	1.04	1.004	1	1.54
Wavelet white noise ^g (mmag)	1.32	0.79	1.91	1.36	1.28
Wavelet red noise ^g (mmag)	0.00	0.22	0.18	0.00	1.52
OoT baseline function	None	Linear	—	—	Linear
Planet	WASP-33b	WASP-33b	WASP-33b	WASP-36b	WASP-36b
Date	2012 December 01	2012 October 01	All	2012 December 29	2013 March 15
Filter ^a	<i>B</i>	<i>U</i>	<i>U</i>	<i>R</i>	<i>U</i>
T_c (HJD-2450000)	6263.8419 ^{+0.0036} _{-0.0076}	6202.847 78 ^{+0.000 67} _{-0.000 69}	—	6290.861 29 ^{+0.000 34} _{-0.000 26}	6367.728 98 ^{+0.000 95} _{-0.000 58}
R_p/R_*	0.1127 ^{+0.0054} _{-0.0056}	0.1017 ^{+0.0027} _{-0.0027}	0.1086 ^{+0.0022} _{-0.0007}	0.13850 ^{+0.00071} _{-0.00082}	0.1316 ^{+0.0018} _{-0.0018}
Duration (min)	167.31 ^{+2.15} _{-2.15}	165.50 ^{+0.71} _{-0.71}	166.94 ^{+0.55} _{-0.55}	109.46 ^{+0.72} _{-0.72}	107.96 ^{+1.41} _{-1.41}
$\beta_{\text{res}2}^b$ (R_p/R_*)	1.44	1.21	2.33	1.24	0.80
$\beta_{\text{res}2}^b$ (Mid)	1.197	1.16	—	1.18	0.75
$\beta_{\text{res}1}^c$ (R_p/R_*)	+0.85 −1.67	2.34 −2.70	+6.95 −3.68	+0.95 −0.41	+0.31 −0.25
$\beta_{\text{res}1}^c$ (Mid)	+3.31 −3.33	+4.11 −2.70	—	+1.59 −0.50	+0.68 −0.43
β_{time}^d	1.05	1.01	1.02	1.002	1.00
White noise ^e (mmag)	6.45 ^{+3.50} _{-3.50}	3.03 ^{+1.31} _{-1.31}	3.21 ^{+1.35} _{-1.35}	1.99 ^{+0.86} _{-0.86}	2.30 ^{+1.02} _{-1.02}
Red noise ^e (mmag)	1.96 ^{+1.71} _{-1.71}	0.28 ^{+0.28} _{-0.28}	0.67 ^{+0.24} _{-0.24}	0.13 ^{+0.68} _{-0.13}	0.00
β_{wave}^f	1.05	1.39	1.14	1.00	1.00
White noise ^g (mmag)	5.13	1.18	1.84	1.80	3.47
Red noise ^g (mmag)	1.58	1.13	1.00	0.01	0.00
OoT baseline function	None	Quadratic	—	Linear	Linear

^aFilter: *B* is the Harris *B* (330–550 nm), *R* is the Harris *R* (550–900 nm), *V* is the Harris *V* (473–686 nm) and *U* is the Bessell *U* (303–417 nm).

^b $\beta_{\text{res}2}$ is found by using the second residual permeation method (Section 3.1.1).

^c $\beta_{\text{res}1}$ is found by using the first residual permeation method (Section 3.1.1).

^d β_{time} is the scaling factor for the time-averaging method (Pont et al. 2006, Section 3.1.1).

^eThe red and white noise are calculated using the time-averaging method (Pont et al. 2006, Section 3.1.1).

^f β_{wave} is the scaling factor for the wavelet likelihood technique (Carter & Winn 2009, Section 3.1.1).

^gThe red and white noise are calculated using the wavelet likelihood technique (Carter & Winn 2009, Section 3.1.1).

where K_* is the radial velocity amplitude of the host star and P_p is the orbital period of the planet. We adopt the formula by Southworth et al. (2007a) to calculate the surface gravitational acceleration, g_p :

$$g_p = \frac{2\pi}{P_p} \left(\frac{a}{R_p} \right)^2 \frac{\sqrt{1-e^2}}{\sin i} K_*. \quad (10)$$

The equilibrium temperature, T_{eq} , is derived using the relation (Southworth 2010):

$$T_{\text{eq}} = T_{\text{eff}} \left(\frac{1-A}{4F} \right)^{1/4} \left(\frac{R_*}{2a} \right)^{1/2}, \quad (11)$$

where T_{eff} is the effective temperature of the host star, A is the Bond albedo, and F is the heat redistribution factor. This formula is simplified by making the assumption, as done in Southworth (2010), that $A = 1 - 4F$; the resulting equation is the modified equilibrium temperature, T'_{eq} :

$$T'_{\text{eq}} = T_{\text{eff}} \left(\frac{R_*}{2a} \right)^{1/2}. \quad (12)$$

The Safronov number, Θ , is a measure of the ability of a planet to gravitationally scatter or capture other bodies in nearby orbits (Safronov 1972). We calculate Θ using the equation from Southworth (2010):

$$\Theta = \frac{M_p a}{M_* R_p}. \quad (13)$$

Differences between Safronov numbers could point to differences in migration or stopping mechanisms (Seager 2011). As defined by Hansen & Barman (2007), Class I hot Jupiters have $\Theta = 0.07 \pm 0.01$ and Class II have $\Theta = 0.04 \pm 0.01$. However, Southworth (2012) find that this division of hot Jupiters into two classes was not evident when using a greater sample of planets. The atmospheric scaleheight, H , is calculated using (de Wit & Seager 2013)

$$H = \frac{k_B T'_{\text{eq}}}{\mu g_b}, \quad (14)$$

Table 10. Parameters derived in this study for the WASP-48b light curve using EXOMOP.

Planet	WASP-48b
Date	2011 October 09
Filter ^a	<i>U</i>
T_c (HJD-2450000)	5844.7249 ^{+0.0019} _{-0.0017}
R_p/R_*	0.0916 ^{+0.0017} _{-0.0017}
Duration (min)	192.20 ^{+1.73} _{-1.73}
$\beta_{\text{res}2}^b$ (R_p/R_*)	1.16
$\beta_{\text{res}2}^b$ (Mid)	1.19
$\beta_{\text{res}1}^c$ (R_p/R_*)	+0.11 –0.98
$\beta_{\text{res}1}^c$ (Mid)	+1.35 –1.24
β_{time}^d	1.00
White noise ^e (mmag)	2.16 ^{+0.96} _{-0.96}
Red noise ^e (mmag)	0.00
β_{wave}^f	1.00
White noise ^g (mmag)	2.22
Red noise ^g (mmag)	0.02
OoT baseline function	None

^aFilter: *B* is the Harris *B* (330–550 nm), *R* is the Harris *R* (550–900 nm), *V* is the Harris *V* (473–686 nm) and *U* is the Bessell *U* (303–417 nm).

^b $\beta_{\text{res}2}$ is found by using the second residual permeation method (Section 3.1.1).

^c $\beta_{\text{res}1}$ is found by using the first residual permeation method (Section 3.1.1).

^d β_{time} is the scaling factor for the time-averaging method (Pont et al. 2006, Section 3.1.1).

^e The red and white noise are calculated using the time-averaging method (Pont et al. 2006, Section 3.1.1).

^f β_{wave} is the scaling factor for the wavelet likelihood technique (Carter & Winn 2009, Section 3.1.1).

^g The red and white noise are calculated using the wavelet likelihood technique (Carter & Winn 2009, Section 3.1.1).

where k_B is Boltzmann’s constant and μ is the mean molecular weight in the planet’s atmosphere (set to 2.3; de Wit & Seager 2013).

4.1 Period determination

By combining our EXOMOP derived mid-transit times with previously published mid-transit times, we refine the orbital period of our targets. When necessary, the mid-transit times are transformed from HJD, which is based on UTC time, into BJD, which is based on Barycentric Dynamical Time (TDB), using the online converter⁹ by Eastman, Siverd & Gaudi (2010). We derive an improved ephemeris for each target by performing a weighted linear least-squares analysis using the following equation:

$$T_c = T_c(0) + P_p \times E, \quad (15)$$

where $T_c(0)$ is the mid-transit time at the discovery epoch in BJD_{TDB}, P_p is the orbital period of the target, and E is the integer number of cycles after their discovery paper. See Tables 13 and 14 for an updated $T_c(0)$ and P_p for each system. The results of the transit timing analysis for all our targets can be found in Table 15 (the entire table can be found online).

⁹ <http://astroutils.astronomy.ohio-state.edu/time/hjd2bjd.html>

5 INDIVIDUAL SYSTEMS

5.1 CoRoT-1b

CoRoT-1b is the first transiting exoplanet discovered by the CoRoT satellite (Baglin 2003; Barge et al. 2008). Several follow-up primary transit photometry studies of the system find no signs of a changing period (Bean 2009; Gillon et al. 2009; Csizmadia et al. 2010; Rauer et al. 2010; Southworth 2011; Sada et al. 2012; Ranjan et al. 2014). CoRoT-1b’s atmosphere may have a temperature inversion (Alonso et al. 2009; Gillon et al. 2009; Rogers et al. 2009; Snellen, de Mooij & Albrecht 2009; Zhao et al. 2012) or an isothermal profile (Deming et al. 2011). Infrared transmission spectroscopy observations by Schlawin et al. (2014) disfavour a TiO/VO-rich spectrum for CoRoT-1b, suggesting the temperature inversion is caused by another absorber in the atmosphere or that flat spectrum is due to clouds or a haze layer. Pont et al. (2010) observed the Rossiter–McLaughlin effect (Winn 2011) for this planet and found that the projected spin-orbit angle is not aligned with the stellar spin axis with $\lambda = 77^\circ \pm 11^\circ$. The Rossiter–McLaughlin effect is important because planets that are not orbiting coplanar with their host stars may exhibit bow shock variability (See Section 6.2.1; Vidotto et al. 2011a; Llama et al. 2013).

We observed CoRoT-1b on 2012 December 07 using the *U* filter (Table 2), which is the first published near-UV light curve of this planet (Fig. 1). Our derived physical parameters (Table 13) agree with previous studies and reduce the uncertainty on the period by a factor of 5 compared to Gillon et al. (2009). We also find a near-UV $R_p/R_* = 0.1439^{+0.0020}_{-0.0018}$ which is 2.3σ larger than its optical $R_p/R_* = 0.1381^{+0.0007}_{-0.0015}$ (Gillon et al. 2009). An early near-UV or any non-spherical asymmetries are not seen in this transit of CoRoT-1b.

5.2 GJ436b

GJ436b, a hot Neptune, was discovered through radial velocity measurements (Butler et al. 2004) and later confirmed to be a transiting exoplanet (Gillon et al. 2007b). There have been extensive ground-based and space-based photometry and spectral studies of the GJ436b (e.g. Deming et al. 2007; Demory et al. 2007; Gillon et al. 2007a,b; Maness et al. 2007; Alonso et al. 2008; Bean et al. 2008; Bean & Seifahrt 2008; Coughlin et al. 2008; Ribas, Font-Ribera & Beaulieu 2008; Southworth 2008, 2010; Cáceres et al. 2009; Figueira et al. 2009; Shporer et al. 2009; Ballard et al. 2010; Gibson et al. 2010; Pont et al. 2010; Ehrenreich, Lecavelier Des Etangs & Delfosse 2011; Knutson et al. 2011, 2014; Shabram et al. 2011; Stevenson et al. 2012; Moses et al. 2013; Gaidos et al. 2014; Kulow et al. 2014; Lanotte et al. 2014; Line et al. 2014). The host star is found to be inactive (e.g. Bean et al. 2006; Torres 2007; Wright et al. 2007; Madhusudhan & Winn 2009; Albrecht et al. 2012; Ballerini et al. 2012; von Braun et al. 2012; Kislyakova et al. 2013) and there are two other transiting planets in the system (Ribas et al. 2008; Ballard et al. 2010; Stevenson et al. 2012; Knutson et al. 2014). The host star being inactive reduces the possibility of bow shock variability in our near-UV observations (Vidotto et al. 2011a; Llama et al. 2013). In our sample, GJ436b has the lowest planetary mass, is the only hot Neptune, and the only planet orbiting an M-dwarf.

We observed the first near-UV light curve of GJ436b on 2012 March 23 and subsequently on 2012 April 07 (Table 2, Fig. 1). The light curves obtained for this object are noisy because the observations are reaching the precision limit for the 1.55-m Kuiper

Table 11. Parameters derived in this study for the HAT-P-13b, WASP-12b, and WASP-44b light curves using EXOMOP.

Parameter	Value	Value	Value	Value
Planet	HAT-P-13b	WASP-12b	WASP-12b	WASP-12b
Date	2013 March 02	2011 November 15	2011 November 15	2012 March 22
Filter ^a	<i>U</i>	<i>U</i>	<i>R</i>	<i>U</i>
T_c (HJD-2450000)	6354.6974 ^{+0.0014} _{-0.0014}	5881.983 75 ^{+0.000 47} _{-0.000 78}	5881.982 29 ^{+0.000 80} _{-0.000 80}	6009.679 29 ^{+0.000 60} _{-0.000 57}
R_p/R_*	0.0850 ^{+0.0022} _{-0.0014}	0.119 63 ^{+0.000 82} _{-0.000 82}	0.1153 ^{+0.0016} _{-0.0016}	0.123 13 ^{+0.000 87} _{-0.000 87}
a/R_*	5.280 ^{+0.065} _{-0.065}	3.189 ^{+0.021} _{-0.021}	3.057 ^{+0.052} _{-0.051}	3.202 ^{+0.025} _{-0.036}
Duration (min)	202.44 ^{+1.38} _{-1.38}	176.44 ^{+3.08} _{-3.08}	180.57 ^{+3.08} _{-3.08}	179.58 ^{+1.39} _{-1.39}
β_{res2}^b (R_p/R_*)	1.48	0.99	1.50	0.70
β_{res2}^b (Mid)	1.35	0.91	1.46	0.70
β_{res2}^b (a/R_*)	1.348	0.91	1.47	0.73
β_{res1}^c (R_p/R_*)	+1.55 – 0.63	+0.49 – 1.01	+1.20 – 1.26	+0.31 – 0.71
β_{res1}^c (Mid)	+0.98 – 1.35	+0.64 – 1.70	+1.23 – 1.99	+0.23 – 0.89
β_{res1}^b (a/R_*)	+0.87 – 0.99	+1.29 – 0.80	+1.75 – 2.01	+1.30 – 0.78
β_{time}^d	1.00	1.00	1.00	1.00
White noise ^e (mmag)	1.67 ^{+0.46} _{-0.46}	1.59 ^{+0.74} _{-0.74}	1.42 ^{+0.65} _{-0.65}	2.31 ^{+0.65} _{-0.65}
Red noise ^e (mmag)	0.00	0.00	0.00	0.00
β_{wave}^f	1.00	1.00	1.00	1.00
White noise ^g (mmag)	1.20	1.22	1.11	1.62
Red noise ^g (mmag)	0.00	0.00	0.00	0.00
OoT baseline function	None	Linear	Linear	Linear
Planet	WASP-12b	WASP-12b	WASP-12b	WASP-44b
Date	2012 October 02	2012 November 30	All	2011 October 13
Filter ^a	<i>U</i>	<i>U</i>	<i>U</i>	<i>U</i>
T_c (HJD-2450000)	6202.953 39 ^{+0.000 45} _{-0.000 55}	6262.888 31 ^{+0.000 68} _{-0.000 68}	–	5848.8477 ^{+0.0013} _{-0.0013}
R_p/R_*	0.116 60 ^{+0.000 77} _{-0.000 77}	0.1193 ^{+0.0014} _{-0.0014}	0.120 16 ^{+0.000 76} _{-0.000 65}	0.1228 ^{+0.0028} _{-0.0028}
a/R_*	3.096 ^{+0.023} _{-0.046}	3.313 ^{+0.046} _{-0.051}	3.217 ^{+0.038} _{-0.026}	8.31 ^{+0.30} _{-0.30}
Duration (min)	179.43 ^{+1.43} _{-1.43}	170.78 ^{+1.31} _{-1.31}	171.26 ^{+2.17} _{-2.17}	135.81 ^{+1.60} _{-1.60}
β_{res2}^b (R_p/R_*)	0.97	1.14	1.87	1.15
β_{res2}^b (Mid)	0.92	1.02	–	1.07
β_{res2}^b (a/R_*)	0.92	1.02	1.27	1.25
β_{res1}^c (R_p/R_*)	+0.77 – 0.41	+1.01 – 1.00	+1.00 – 1.40	+0.25 – 0.28
β_{res1}^c (Mid)	+0.92 – 1.23	+0.95 – 0.91	–	0.86 – 0.72
β_{res1}^b (a/R_*)	+0.56 – 1.97	+1.15 – 1.16	+2.03 – 1.61	0.87 – 0.53
β_{time}^c	1.02	1.00	1.00	1.00
White noise ^e (mmag)	2.07 ^{+0.91} _{-0.91}	3.35 ^{+1.32} _{-1.32}	2.51 ^{+1.31} _{-1.31}	5.05 ^{+1.70} _{-1.70}
Red noise ^e (mmag)	0.15 ^{+0.15} _{-0.15}	0.00	0.00	0.00
β_{wave}^f	1.00	1.00	1.00	1.00
Wavelet white noise ^g (mmag)	1.56	3.23	2.06	5.25
Wavelet red noise ^g (mmag)	0.001	0.00	0.00	0.00
OoT baseline function	Linear	Linear	–	Linear

^aFilter: *B* is the Harris *B* (330–550 nm), *R* is the Harris *R* (550–900 nm), *V* is the Harris *V* (473–686 nm) and *U* is the Bessell *U* (303–417 nm).

^b β_{res2} is found by using the second residual permeation method (Section 3.1.1).

^c β_{res1} is found by using the first residual permeation method (Section 3.1.1).

^d β_{time} is the scaling factor for the time-averaging method (Pont et al. 2006, Section 3.1.1).

^eThe red and white noise are calculated using the time-averaging method (Pont et al. 2006, Section 3.1.1).

^f β_{wave} is the scaling factor for the wavelet likelihood technique (Carter & Winn 2009, Section 3.1.1).

^gThe red and white noise are calculated using the wavelet likelihood technique (Carter & Winn 2009, Section 3.1.1).

telescope due to the small transit depth and the faintness of the M-dwarf in the near-UV (these observations are $\sim 2 \times$ the photon limit). However, there are no non-spherical asymmetries in the near-UV lights of GJ436b. Our physical parameters (Table 13) and light-curve solution (Table 8) are consistent with previous studies. We find a near-UV $R_p/R_* = 0.0758^{+0.0086}_{-0.0075}$ which is consistent within 1σ of its optical $R_p/R_* = 0.083 \pm 0.000 27$ (Knutson et al. 2014).

5.3 HAT-P-1b

HAT-P-1b is the first planet discovered by the HATNet project (Bakos et al. 2002, 2007) and the planet orbits one of the stars in a

visual binary (Bakos et al. 2007; Liu et al. 2014). There have been many follow-up transit observations of HAT-P-1b (e.g. Winn et al. 2007; Johnson et al. 2008; Todorov et al. 2010; Sada et al. 2012; Wilson et al. 2015). Secondary eclipse measurements by Béky et al. (2013) found a 2σ upper limit of 0.64 for HAT-P-1b's geometric albedo between 577 and 947 nm. Nikolov et al. (2014) found a conclusive detection of both sodium and water in the transmission spectra using the Space Telescope Imaging Spectrograph onboard the *HST*. Rossiter–McLaughlin effect measurements of the system found that HAT-P-1b is aligned ($3^\circ \pm 2^\circ$) with the host star's equator (Johnson et al. 2008). HAT-P-1b has the longest orbital period of all the planets in our study.

Table 12. Parameters derived in this study for the WASP-44b and WASP-77Ab light curves using EXOMOP.

Parameter	Value	Value	Value
Planet	WASP-44b	WASP-44b	WASP-77Ab
Date	2013 October 19	2013 October 09	2012 December 06
Filter ^a	<i>B</i>	<i>V</i>	<i>U</i>
T_c (HJD-2450000)	6585.685 80 ^{+0.000 63} _{-0.000 63}	6585.686 18 ^{+0.000 77} _{-0.000 53}	6271.658 04 ^{+0.000 32} _{-0.000 35}
R_p/R_*	0.1236 ^{+0.0019} _{-0.0019}	0.1164 ^{+0.0017} _{-0.0017}	0.126 12 ^{+0.000 98} _{-0.000 94}
a/R_*	8.59 ^{+0.11} _{-0.12}	8.33 ^{+0.09} _{-0.14}	5.396 ^{+0.054} _{-0.054}
Duration (min)	126.21 ^{+2.73} _{-2.73}	129.10 ^{+2.84} _{-2.84}	129.67 ^{+1.61} _{-1.61}
β_{res2}^b (R_p/R_*)	1.04	1.23	1.69
β_{res2}^b (Mid)	1.04	1.26	1.55
β_{res2}^b (a/R_*)	1.01	1.21	1.47
β_{res1}^c (R_p/R_*)	+0.11 -0.14	+0.92 -0.75	0.36 -0.53
β_{res1}^c (Mid)	+0.58 -0.49	+1.62 -1.03	1.07 -0.87
β_{res1}^c (a/R_*)	+0.44 -0.32	+0.96 -1.77	1.00 -1.33
β_{time}^d	1.00	1.00	1.00
White noise ^e (mmag)	2.18 ^{+1.06} _{-1.06}	2.04 ^{+1.02} _{-1.02}	1.53 ^{+0.51} _{-0.51}
Red noise ^e (mmag)	0.00	0.00	0.00
β_{wave}^f	1.00	1.00	1.00
White noise ^g (mmag)	2.45	2.18	1.34
Red noise ^g (mmag)	0.00	0.00	0.00
OoT baseline function	Linear	Linear	Linear

^aFilter: *B* is the Harris *B* (330–550 nm), *R* is the Harris *R* (550–900 nm), *V* is the Harris *V* (473–686 nm) and *U* is the Bessell *U* (303–417 nm).

^b β_{res2} is found by using the second residual permeation method (Section 3.1.1).

^c β_{res1} is found by using the first residual permeation method (Section 3.1.1).

^d β_{time} is the scaling factor for the time-averaging method (Pont et al. 2006, Section 3.1.1).

^eThe red and white noise are calculated using the time-averaging method (Pont et al. 2006, Section 3.1.1).

^f β_{wave} is the scaling factor for the wavelet likelihood technique (Carter & Winn 2009, Section 3.1.1).

^gThe red and white noise are calculated using the wavelet likelihood technique (Carter & Winn 2009, Section 3.1.1).

The first near-UV light curve of HAT-P-1b was observed on 2012 October 02 (Table 2, Fig. 1). The stellar binary was used as the main reference star in our light-curve analysis since the two stars are nearly identical in their stellar parameters (Bakos et al. 2007; Liu et al. 2014) and will experience similar variations due to the atmosphere (the stars are only separated by 11 arcsec). Our light-curve solution (Table 8) and derived planetary parameters (Table 13) agree with previous studies. We find a near-UV $R_p/R_* = 0.1189^{+0.0010}_{-0.0015}$ which is within 1σ of the optical $R_p/R_* = 0.118 02 \pm 0.000 18$ (Nikolov et al. 2014). We do not observe an early ingress or any non-spherical asymmetries in the light curve of HAT-P-1b.

5.4 HAT-P-13b

HAT-P-13b, is an inflated hot Jupiter in a nearly circular orbit (Bakos et al. 2009) and the system also has a massive outer planet ($M_{p,c} \sin i_c = 14.3 M_{Jup}$; Winn et al. 2010; Knutson et al. 2014), on a highly eccentric orbit (Bakos et al. 2009). Follow-up photometry studies have refined the planetary parameters of HAT-P-13b and searched for possible transit timing variations (Szabó et al. 2010; Winn et al. 2010; Fulton et al. 2011; Pál et al. 2011; Nascimbeni et al. 2011; Southworth et al. 2012a; Sada & Ramón-Fox 2016). In addition, Winn et al. (2010) performed Rossiter–McLaughlin effect measurements of the system and found that HAT-P-13b is likely aligned ($1^\circ 9 \pm 8^\circ 6$) with its host star's equator. HAT-P-13 has the highest metallicity of all the host stars in our sample.

We observed the first near-UV transit of HAT-P-13b on 2013 March 02 (Table 2, Fig. 1). Our light curve (Table 11) and physical parameters (Table 13) agree with previous studies and the error on our period is improved by a factor of 1.6 over the error found by Southworth et al. (2012a). We find a near-UV R_p/R_*

$= 0.0850^{+0.0022}_{-0.0014}$, which is consistent with its optical $R_p/R_* = 0.0871 \pm 0.0024$ (Southworth et al. 2012a). Turner et al. (2013) suggest that their non-detection of a bow shock around TrES-3b could have caused by the low metallicity of the host star. Therefore, HAT-P-13b is an important target to test this suggestion since it has a high metallicity. Despite HAT-P-13 having a high metallicity, we do not observe an early near-UV ingress.

5.5 HAT-P-16b

HAT-P-16b is a hot Jupiter with a radius of $1.289 \pm 0.066 R_{Jup}$ and an abnormally large mass of $4.193 \pm 0.094 M_{Jup}$ (Buchhave et al. 2010). Spectroscopic and photometric studies have confirmed and improved upon the discovery values (Husnoo et al. 2012; Ciceri et al. 2013; Pearson et al. 2014; Sada & Ramón-Fox 2016). It was found through Rossiter–McLaughlin observations (Moutou et al. 2011) that HAT-P-16b's projected spin-orbit angle of $\lambda = -10^\circ \pm 16^\circ$ is aligned with the stellar spin axis. HAT-P-16b has the highest planetary mass in our sample.

We observed the second near-UV transit of HAT-P-16b on 2013 November 02 using the near-UV filter (Table 2, Fig. 2). This near-UV transit is observed to follow-up the observations done by Pearson et al. (2014). We perform a combined analysis with our near-UV transit and the near-UV transit presented by Pearson et al. (2014) since they used the same telescope/filter and the data reduction pipeline (EXODRPL) as we do in this study. This combined light curve is binned by 2 min to minimize the contribution of red noise. Our light-curve solution (Table 8) and derived planetary parameters (Table 13) agree with previous studies. The error on our period improved by a factor of 2 over that presented by Pearson et al. (2014). We also find a near-UV radius of $R_p/R_* = 0.106 45 \pm 0.000 67$, which

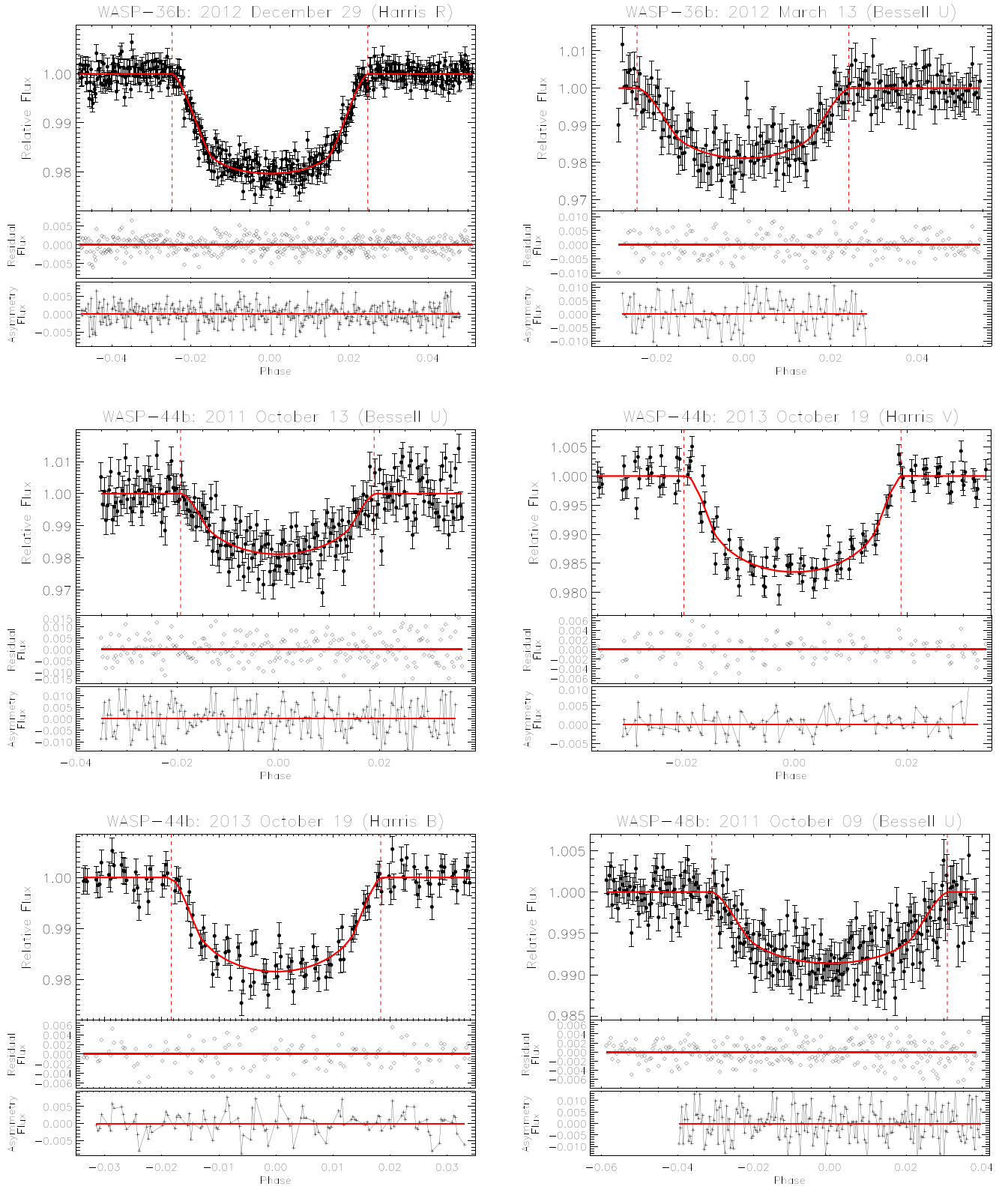


Figure 6. Light curves of WASP-36b, WASP-44b, and WASP-48b. Other comments are the same as Fig. 1.

is consistent within 1σ of its optical radius $R_p/R_* = 0.1071 \pm 0.0014$ (Ciceri et al. 2013). The near-UV light curves used in this study are stable (the R_p/R_* values are constant) over the ~ 1 yr time period observed.

A very extended planetary magnetosphere (Vidotto et al. 2011c, see fig. 9) or a clumpy magnetosheath could cause a double transit to occur if the material absorbing the near-UV radiation is concentrated in a small area. Specifically, if the absorbing material

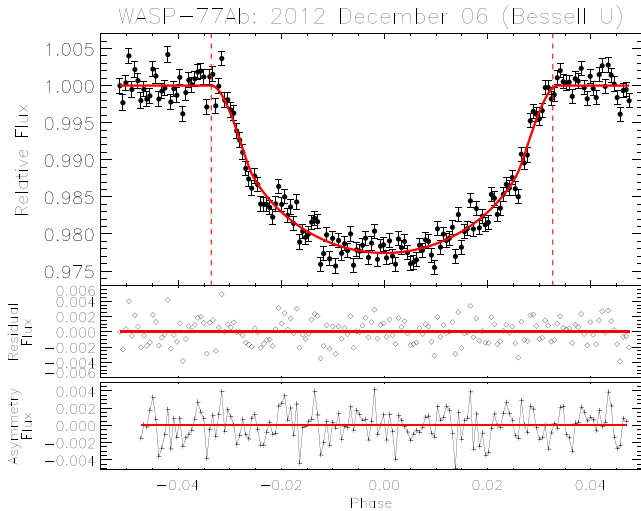


Figure 7. Light curve of WASP-77Ab. Other comments are the same as Fig. 1.

does not fill the entire planetary magnetosphere then there will be a gap between the absorbing material and the planetary radius (thus causing a double transit). The early ingress scenario described in the introduction assumes a filled planetary magnetosphere (constant absorption from the planet to the bow-shock) resulting in a blended absorption light curve. Pearson et al. (2014) suggest they may have observed a double transit in their 2012 December 29 near-UV data of HAT-P-16b at a phase of -0.0305 or ~ 26 min before the start of ingress (see their fig. 1). These authors cautioned that this 2σ feature requires follow-up observations. Our observations of HAT-P-16b do not reproduce this characteristic. Therefore, we believe the feature seen by Pearson et al. (2014) may have been an unknown systematic in their data set or is temporal.

5.6 HAT-P-22b

HAT-P-22b, a hot Jupiter, was discovered by Bakos et al. (2011) around a G5 star that is part of a binary system with a distant M-dwarf companion (Bakos et al. 2011; Knutson et al. 2014). This planet is a pL class exoplanet as defined by the Fortney et al. (2008) due to a low incoming flux impinging on its atmosphere. The host star of HAT-P-22b has the lowest mass of the hot Jupiter hosting stars in our sample.

We observed the first follow-up light curves of HAT-P-22b on 2013 February 22 and 2013 March 22 using the *U* filter (Table 2, Fig. 2). We combined the near-UV data and binned it by 2 min (this time was chosen to minimize the contribution of red noise). The derived planetary parameters agree with the discovery values and the error on the period is improved by a factor of 7.5 (Table 13). We also find a near-UV radius of $R_p/R_* = 0.1079 \pm 0.00094$, which is consistent with its optical $R_p/R_* = 0.1065 \pm 0.0017$ (Bakos et al. 2011). Any non-spherical asymmetries are not seen in our data.

5.7 TrES-2b

The hot Jupiter TrES-2b was the first transiting planet discovered in the Kepler field (O'Donovan et al. 2006). Follow-up transit observations have confirmed and refined the planetary parameters of this system (Holman et al. 2007; Colón et al. 2010; Croll et al. 2010; Gilliland et al. 2010; Mislis et al. 2010; O'Donovan et al. 2010; Scuderi et al. 2010; Southworth 2011; Kipping & Bakos 2011; Kip-

ping & Spiegel 2011; Christiansen et al. 2011; Barclay et al. 2012; Schröter, Schmitt & Müller 2012; Esteves et al. 2013; Ranjan et al. 2014). In addition, Rossiter–McLaughlin effect measurements of the system found that TrES-2b is aligned with its host star's equator ($-9^\circ \pm 12^\circ$) and orbits in a prograde orbit (Winn et al. 2008a). TrES-2b has the lowest albedo of any exoplanet currently known (Kipping & Spiegel 2011).

We observed the first near-UV light curve of TrES-2b on 2012 October 29 (Table 2, Fig. 2). There is non-clear evidence for any non-spherical asymmetries in TrES-2b. The TrES-2 system parameters were measured by Esteves et al. (2013) using 3 yr of observations by the *Kepler* spacecraft. Due to their extensive analysis, we choose to only derive the near-UV radius of the planet (Table 13). We find a near-UV $R_p/R_* = 0.1243 \pm 0.0024$, which is consistent with its optical $R_p/R_* = 0.125358^{+0.000019}_{-0.000024}$ (Esteves et al. 2013).

5.8 TrES-4b

The hot Jupiter TrES-4b has a very low density and is one of the most highly inflated transiting giant planets known to date (Mandushev et al. 2007). Primary transit follow-up studies have refined these planetary parameters and searched for transit timing variations (Torres et al. 2008; Sozzetti et al. 2009, 2015; Southworth 2010; Chan et al. 2011; Sada et al. 2012; Ranjan et al. 2014). TrES-4b was found to be aligned ($6.3 \pm 4.7^\circ$) with its host star's equator using measurements of the Rossiter–McLaughlin effect (Narita et al. 2010). This system has the largest planetary radius and largest host star mass and radius in our sample.

Our observations of TrES-4b were conducted on 2011 July 26 using the Bessell *U* and Harris *R* filters (Table 2). We present the only published near-UV light curve of TrES-4b (Fig. 5, Table 8). Our planetary parameters agree with the discovery values and improve the error on the period by a factor of 2.3 (Table 13). We also find a near-UV $R_p/R_* = 0.1094^{+0.0052}_{-0.0052}$, which is larger by 2σ of its optical $R_p/R_* = 0.09745 \pm 0.00076$ (Chan et al. 2011). We do not observe any non-spherical asymmetries in our data due to the presence of an optically thick bow shock.

5.9 WASP-1b

WASP-1b is the first exoplanet discovered by the SuperWASP survey (Pollacco et al. 2006; Collier Cameron et al. 2007). Several follow-up photometry studies that have refined these planetary parameters and searched for transit timing variations (Charbonneau et al. 2007; Shporer et al. 2007; Southworth 2008, 2012; Szabó et al. 2010; Sada et al. 2012; Granata et al. 2014; Maciejewski et al. 2014). Wheatley et al. (2010) observed the secondary transit of WASP-1b and found a strong temperature inversion in its atmosphere and ineffective day–night energy redistribution. Rossiter–McLaughlin effect measurements found WASP-1b to be misaligned with the equator of its host star (Stempels et al. 2007; Albrecht et al. 2011; Simpson et al. 2011). WASP-1 is the only F star (F7V) in our sample.

Here, we present the first near-UV light curves of WASP-1b (Tables 2, 8 and 9, Fig. 3). The light-curve solution (Tables 8 and 9) and the derived planetary parameters (Table 13) are in agreement to previous studies. We also find a near-UV radius of $R_p/R_* = 0.0964 \pm 0.0010$, which is smaller by 3.5σ with its optical radius of $R_p/R_* = 0.1048 \pm 0.0014$ (Granata et al. 2014). We do not see an early ingress or any non-spherical asymmetries in our near-UV transits. Our near-UV light curves are stable over the 1 month time period observed.

Table 13. Physical properties of CoRoT-1b, GJ436b, HAT-P-1b, HAT-P-13b, HAT-P-22b, TrES-2b, TrES-4b, and WASP-1b derived from the light-curve modelling. References. – (1) Our Study; (2) Gillon et al. (2009); (3) Knutson et al. (2014); (4) Nikolov et al. (2014); (5) Southworth et al. (2012a); (6) Winn et al. (2010); (7) Ciceri et al. (2013); (8) Husnoo et al. (2012); (9) Bakos et al. (2011); (10) Barclay et al. (2012); (11) Chan et al. (2011); (12) Maciejewski et al. (2014); (13) Stempels et al. (2007).

Parameter (units)	Value	Source	Value	Source	Value	Source
Planet	CoRoT-1b	–	GJ436b	–	HAT-P-1b	–
M_b (M_{Jup})	1.07 ± 0.17	1	0.0728 ± 0.0024	1	0.529 ± 0.020	1
Near-UV R_p/R_*	$0.1439^{+0.0020}_{-0.0018}$	1	$0.0758^{+0.0086}_{-0.0075}$	1	$0.1189^{+0.0010}_{-0.0015}$	1
Optical R_p/R_*	$0.1381^{+0.0007}_{-0.0015}$	2	$0.08310 \pm 0.000\ 27$	3	$0.118\ 02 \pm 0.000\ 18$	4
Near-UV R_b (R_{Jup})	1.48 ± 0.13	1	0.342 ± 0.041	1	1.358 ± 0.036	1
Optical R_b (R_{Jup})	1.42 ± 0.24	2	0.3739 ± 0.0097	3	1.319 ± 0.019	4
ρ_b (ρ_{Jup})	0.33 ± 0.10	1	1.30 ± 0.11	1	0.269 ± 0.040	1
$\log g_b$ (cgs)	3.12 ± 0.20	1	3.180 ± 0.032	1	2.912 ± 0.048	1
T_{eq} (K)	1834 ± 46	2	686 ± 10	3	1322 ± 15	4
H (km)	705 ± 320	1	230 ± 17	1	1008 ± 73	1
Θ	0.039 ± 0.013	1	0.0267 ± 0.0015	1	0.0403 ± 0.0032	1
Orbital inclination ($^\circ$)	$85.66^{+0.62}_{-0.48}$	2	86.774 ± 0.030	3	85.634 ± 0.056	4
Orbital eccentricity	$0.071^{+0.62}_{-0.48}$	2	0.150 ± 0.012	3	0.00	4
a (au)	$0.0259^{+0.0011}_{-0.0020}$	2	$0.03109 \pm 0.000\ 74$	3	$0.05561 \pm 0.000\ 83$	4
Period (d)	$1.508\ 976\ 552 \pm 0.000\ 000\ 097$	1	$2.643\ 897\ 88 \pm 0.000\ 000\ 10$	1	$4.465\ 2968 \pm 0.000\ 0018$	1
T_c (0) (BJD)	$2454\ 138.303\ 971 \pm 0.000036$	1	$2454\ 238.479\ 958 \pm 0.000\ 039$	1	$2453\ 979.931\ 65 \pm 0.000\ 25$	1
Planet	HAT-P-13b	–	HAT-P-16b	–	HAT-P-22b	–
M_b (M_{Jup})	0.906 ± 0.023	1	4.189 ± 0.092	1	2.148 ± 0.062	1
Near-UV R_p/R_*	$0.0850^{+0.0022}_{-0.0014}$	1	$0.106\ 45 \pm 0.000\ 67$	1	$0.1079 \pm 0.000\ 94$	1
Optical R_p/R_*	$0.087\ 0498 \pm 0.0024$	5	0.1071 ± 0.0014	7	0.1065 ± 0.0017	9
Near-UV R_b (R_{Jup})	1.452 ± 0.052	1	1.28 ± 0.056	1	1.092 ± 0.047	1
Optical R_b (R_{Jup})	1.487 ± 0.038	5	1.190 ± 0.035	7	1.080 ± 0.058	9
ρ_b (ρ_{Jup})	0.272 ± 0.021	1	1.86 ± 0.24	1	1.61 ± 0.21	1
$\log g_b$ (cgs)	3.008 ± 0.032	1	3.858 ± 0.053	1	3.691 ± 0.063	1
T_{eq} (K)	1740 ± 27	1	1571 ± 21	7	1463 ± 19	9
H (km)	863 ± 65	1	109 ± 13	1	150 ± 22	1
Θ	0.0405 ± 0.0023	1	0.237 ± 0.017	1	0.186 ± 0.017	1
Orbital inclination ($^\circ$)	81.93 ± 0.26	5	87.74 ± 0.59	7	$86.9^{+0.6}_{-0.5}$	9
Orbital eccentricity	0.0133 ± 0.0041	6	0.034 ± 0.003	8	0.016 ± 0.009	9
a (au)	0.0431 ± 0.0012	1	$0.041\ 30 \pm 0.000\ 47$	7	0.0414 ± 0.0005	9
Period (d)	$2.916\ 2382 \pm 0.000\ 0016$	1	$2.775\ 970\ 244 \pm 0.000\ 000\ 66$	1	$3.212\ 2312 \pm 0.000\ 0012$	1
T_c (0) (BJD)	$2455\ 176.538\ 64 \pm 0.00023$	1	$2455\ 027.592\ 939 \pm 0.00019$	1	$2454\ 930.222\ 96 \pm 0.000\ 25$	1
Planet	TrES-2b	–	TrES-4b	–	WASP-1b	–
M_b (M_{Jup})	1.44 ± 0.21	10	0.917 ± 0.070	1	0.846 ± 0.054	1
Near-UV R_p/R_*	0.1243 ± 0.0024	1	$0.1094^{+0.0052}_{-0.0052}$	1	$0.0964^{+0.0010}_{-0.0010}$	1
Optical R_p/R_*	$0.125\ 358^{+0.000019}_{-0.000024}$	10	$0.097\ 45 \pm 0.000\ 76$	11	0.1013 ± 0.0018	1
Near-UV R_b (R_{Jup})	1.215 ± 0.049	1	1.91 ± 0.11	1	1.379 ± 0.033	1
Optical R_b (R_{Jup})	$1.245^{+0.045}_{-0.041}$	10	1.706 ± 0.056	11	1.449 ± 0.041	1
ρ_b (ρ_{Jup})	1.82 ± 0.23	10	0.173 ± 0.022	1	$0.260\ 22 \pm 0.028$	1
$\log g_b$ (cgs)	3.798 ± 0.046	10	2.89 ± 0.055	1	2.998 ± 0.039	1
T_{eq} (K)	1472 ± 12	10	1778 ± 22	11	1812 ± 14	1
H (km)	118 ± 12	1	1373 ± 167	1	920 ± 82	1
Θ	0.216 ± 0.020	10	0.0393 ± 0.0038	1	0.0366 ± 0.0034	1
a (au)	$0.0367^{+0.0013}_{-0.0012}$	10	$0.050\ 84 \pm 0.000\ 50$	11	$0.038\ 89^{+0.00053}_{-0.00073}$	12
Orbital inclination ($^\circ$)	$83.8646^{+0.0041}_{-0.0036}$	10	82.81 ± 0.37	11	88.65 ± 0.55	13
Orbital eccentricity	$0\ 0.0002^{+0.0010}_{-0.0002}$	10	0	11	0	13
Period (d)	$2.470\ 6132 \pm 0.000\ 0001$	10	$3.553\ 9246 \pm 0.000\ 0014$	1	$2.519\ 945\ 29 \pm 0.000\ 000\ 56$	1
T_c (0) (BJD)	$2454\ 969.396\ 61 \pm 0.0048$	10	$2454\ 223.798\ 50 \pm 0.000\ 32$	1	$2453\ 912.515\ 04 \pm 0.000\ 35$	1

5.10 WASP-12b

WASP-12b is a hot Jupiter orbiting a G0 star with a short orbital period (Hebb et al. 2009). There have been extensive photometric and spectroscopic studies of WASP-12b (López-Morales et al. 2010; Campo et al. 2011; Chan et al. 2011; Croll et al. 2011; Husnoo et al. 2011; Maciejewski et al. 2011, 2013; Madhusudhan et al. 2011;

Cowan et al. 2012; Crossfield, Hansen & Barman 2012; Haswell et al. 2012; Sada et al. 2012; Sokov et al. 2012; Southworth et al. 2012b; Zhao et al. 2012; Copperwheat et al. 2013; Crossfield et al. 2013; Föhrling et al. 2013; Fossati et al. 2013; Mandell et al. 2013; Sing et al. 2013; Swain et al. 2013; Bechter et al. 2014; Stevenson et al. 2014a,b; Teske et al. 2014; Burton et al. 2015; Collins,

Table 14. Physical properties of WASP-12b, WASP-33b, WASP-36b, WASP-44b, WASP-48b, and WASP-77Ab derived from the light-curve modelling. References. – (1) Our Study; (2) Maciejewski et al. (2013); (3) Kovács et al. (2013); (4) Collier Cameron et al. (2010); (5) Smith et al. (2011); (6) Anderson et al. (2012); (7) Enoch et al. (2011); (8) Maxted et al. 2013.

Parameter (units)	Value	Source	Value	Source	Value	Source
Planet	WASP-12b	–	WASP-33b	–	WASP-36b	–
M_b (M_{Jup})	2.01 ± 0.14	1	3.28 ± 0.73	1	2.286 ± 0.066	1
Near-UV R_p/R_*	$0.120 \ 16^{+0.00076}_{-0.00065}$	1	$0.1086^{+0.0022}_{-0.0007}$	1	$0.1316^{+0.0018}_{-0.0018}$	1
Optical R_p/R_*	0.1173 ± 0.0005	2	0.1143 ± 0.0002	3	$0.138 \ 50^{+0.00071}_{-0.00082}$	1
Near-UV R_b (R_{Jup})	1.835 ± 0.08	1	$1.594^{+0.043}_{-0.043}$	1	1.218 ± 0.028	1
Optical R_b (R_{Jup})	1.860 ± 0.090	2	$1.679^{+0.019}_{-0.030}$	3	1.281 ± 0.026	1
ρ_b (ρ_{Jup})	0.326 ± 0.049	1	0.65 ± 0.14	1	1.017 ± 0.068	1
$\log g_b$ (cgs)	3.210 ± 0.057	1	3.459 ± 0.098	1	3.538 ± 0.028	1
T'_{eq} (K)	2483 ± 79	1	2723 ± 37	4	1724 ± 39	5
H (km)	773 ± 103	1	477 ± 108	1	252 ± 17	1
Θ	0.0389 ± 0.0055	1	0.065 ± 0.015	1	0.0905 ± 0.0047	1
a (au)	0.0235 ± 0.0011	1	$0.0259^{+0.0005}_{-0.0005}$	3	$0.026 \ 43 \pm 0.000 \ 26$	5
Orbital inclination ($^\circ$)	$82.96^{+0.50}_{-0.44}$	2	86.2 ± 0.2	3	83.61 ± 0.21	5
Orbital eccentricity	0.0447 ± 0.0043	2	0	3	0	5
Period (d)	$1.091 \ 421 \ 19 \pm 0.000 \ 000 \ 21$	1	$1.219 \ 870 \ 16 \pm 0.00014$	1	$1.537 \ 364 \ 23 \pm 0.000 \ 000 \ 57$	1
$T_c(0)$ (BJD)	$2455 \ 147.458 \ 20 \pm 0.000 \ 13$	1	$2452 \ 984.829 \ 64 \pm 0.000 \ 30$	1	$2455 \ 569.838 \ 17 \pm 0.000 \ 10$	1
Planet	WASP-44b	–	WASP-48b	–	WASP-77Ab	–
M_b (M_{Jup})	0.867 ± 0.064	1	0.984 ± 0.085	1	1.76 ± 0.057	1
Near-UV R_p/R_*	0.1228 ± 0.0028	1	0.0916 ± 0.0017	1	$0.1305^{+0.0010}_{-0.0010}$	1 ^a
Optical R_p/R_*	0.1164 ± 0.0017	1	0.0980 ± 0.0010	7	$0.130 \ 12 \pm 0.000 \ 65$	8
Near-UV R_b (R_{Jup})	1.03 ± 0.038	1	1.560 ± 0.088	1	1.21 ± 0.02	1
Optical R_b (R_{Jup})	0.98 ± 0.032	1	1.67 ± 0.10	7	1.21 ± 0.02	8
ρ_b (ρ_{Jup})	0.86 ± 0.11	1	0.198 ± 0.039	1	0.928 ± 0.055	1
$\log g_b$ (cgs)	3.35 ± 0.05	1	2.941 ± 0.092	1	3.471 ± 0.022	1
T'_{eq} (K)	1304 ± 36	6	2035 ± 52	7	1674 ± 24	1
H (km)	292 ± 32	1	1178 ± 415	1	286 ± 59	1
Θ	0.0664 ± 0.0068	1	0.0340 ± 0.0046	1	0.0694 ± 0.0043	1
a (au)	$0.034 \ 43 \pm 0.000 \ 99$	6	0.0344 ± 0.0026	7	$0.023 \ 96 \pm 0.000 \ 43$	1
Orbital inclination ($^\circ$)	86.59	6	80.09 ± 0.55	7	89.40 ± 0.7	8
Orbital eccentricity	0	6	0	7	0	8
Period (d)	$2.423 \ 8120 \pm 0.000 \ 0012$	1	$2.143 \ 635 \ 92 \pm 0.000 \ 0046$	1	$1.360 \ 0306 \pm 0.000 \ 0012$	1
$T_c(0)$ (BJD)	$2455 \ 434.376 \ 55 \pm 0.000 \ 20$	1	$2455 \ 364.552 \ 17 \pm 0.000 \ 20$	1	$2455 \ 870.449 \ 77 \pm 0.000 \ 14$	1

^aThe near-UV R_p/R_* of WASP-77Ab is corrected for the dilution of the companion stars (Section 5.15).**Table 15.** Results of the transit timing analysis.^a

Planet name	T_c (BJD _{TDB})	T_c error (d)	Epoch	O-C (d)	O-C error (d)	Source
CoRoT-1b	2456268.990397	0.00013	1412	0.000 0060	0.000 135	This paper
CoRoT-1b	2454138.328594	0.00039	0	0.000 222	0.000 392	Csizmadia et al. (2010)

^aThis table is available in its entirety in machine-readable form in the online journal. A portion is shown here for guidance regarding its form and content.

Kielkopf & Stassun 2015; Croll et al. 2015; Kreidberg et al. 2015). WASP-12 is a triple star system with a binary M dwarf system in orbit around the G0 star (Crossfield et al. 2012; Bergfors et al. 2013; Bechter et al. 2014). Previous studies by Fossati et al. (2010), Haswell et al. (2012), and Nichols et al. (2015) observed an early near-UV ingress with *HST* using the Cosmic Origins Spectrograph. However, these studies have a low number of data points and therefore follow-up near-UV studies are needed. Ground-based near-UV observations (Copperwheat et al. 2013) and additional space-based UV observations of WASP-12b using the Space Telescope Imaging Spectrograph instrument on *HST* (Sing et al. 2013) all do not observe any asymmetries in their near-UV light curves. Finally, WASP-12b has the closest orbital distance and planetary radius in our study and is the top candidate predicted by VJH11a to exhibit an early near-UV ingress.

Our observations were conducted from 2011 November to 2012 November (Tables 2 and 11; Fig. 4). These observations were performed to follow-up the previous near-UV observations and to confirm the detection of an early ingress. We did not account for the M-dwarf companions in our analysis, because they contribute a negligible amount of flux at the wavelengths observed (Copperwheat et al. 2013). We combined all the near-UV transits and binned the light curve by 1 min and 30 s (this time was chosen to minimize the dominance of red noise). The derived planetary parameters (Table 14) are in agreement to previous studies. Our near-UV radius is within 1σ of that found by Copperwheat et al. (2013) and Sing et al. (2013). We also find a near-UV $R_p/R_* = 0.120 \ 16^{+0.00076}_{-0.00065}$, which is 2.5σ larger than optical radius of $R_p/R_* = 0.1173 \pm 0.0005$ (Maciejewski et al. 2013). The larger near-UV radius is consistent with Rayleigh scattering (Section 6.2). We do not observe an early

ingress in any of our near-UV light curves. Our near-UV light curves are stable over the ~ 1 yr time period observed.

5.11 WASP-33b

WASP-33b is a hot Jupiter (Collier Cameron et al. 2010) that orbits a bright (V -mag = 8.3) δ Scuti variable host star (Herrero et al. 2011). It is the first planet discovered to orbit an A-type star (Herrero et al. 2011). This system has been extensively studied with photometry and spectroscopy (Herrero et al. 2011; Moya et al. 2011; Smith et al. 2011; Deming et al. 2012; Sada et al. 2012; de Mooij et al. 2013; von Essen et al. 2014; Hardy et al. 2015; Haynes et al. 2015; Johnson et al. 2015; von Essen et al. 2015). Secondary eclipse measurements indicate that WASP-33b has a low albedo (de Mooij et al. 2013) and inefficient heat-transport from the day-side to the night-side (Smith et al. 2011; Deming et al. 2012; Madhusudhan 2012; de Mooij et al. 2013; Haynes et al. 2015). In our study, WASP-33b has the highest planetary equilibrium temperature and is the only planet around an A star.

We observed the first near-UV light curve of WASP-33b on 2012 October 01 and subsequently in the B and U bands on 2012 December 01 (Table 2, Fig. 5). We did not take into account the pulsations in our modelling because it was found by von Essen et al. (2014) that taking them into account did not change their final parameter results. We see the variability of the host star in our transits, residuals, and asymmetry test very clearly. The light-curve solution (Table 9) and derived physical parameters (Table 14) are consistent with previous studies (e.g. Collier Cameron et al. 2010; Kovács et al. 2013; von Essen et al. 2014). We find a near-UV $R_p/R_* = 0.1086^{+0.0022}_{-0.0007}$, which is consistent with its optical $R_p/R_* = 0.1066 \pm 0.0009$ (Collier Cameron et al. 2010). There are non-spherical asymmetries in our light curves, however, the amplitude and shape of the variability in the residuals are due to host star's variability. Our near-UV transits are stable over the several months observed.

5.12 WASP-36b

The hot Jupiter WASP-36b was discovered around a G2 dwarf (Smith et al. 2012). Very recent follow-up photometric observations were performed by Mancini et al. (2016) and Maciejewski et al. (2016). The host star shows low levels of stellar activity and has undergone little or no tidal spin-up due to the planet (Smith et al. 2012). WASP-36 has the lowest metallicity of all the hot Jupiter host stars in our sample.

We observed the first near-UV light curve of WASP-36b on 2012 December 29 and an additional R band transit on 2013 March 15 (Tables 2 and 9, Fig. 6). The derived physical parameters (Table 14) agree with the discovery values and the error on the period is improved by a factor of 4.7. We also find a near-UV radius of $R_p/R_* = 0.1316^{+0.0018}_{-0.0018}$ which is 2.6σ smaller than the optical radius of $R_p/R_* = 0.13850^{+0.00071}_{-0.00082}$.

5.13 WASP-44b

The hot Jupiter WASP-44b is a highly inflated planet in orbit around a G8V star (Anderson et al. 2012). The host star, WASP-44, is found to be inactive based off observations of weak Ca II H&K emission and no rotational modulation (Anderson et al. 2012). The first follow-up light curve of WASP-44b (Mancini et al. 2013) indicates a constant radius from the optical to NIR wavelengths. This system has the smallest host star radius of all hot Jupiter systems in our study.

We observed the first near-UV light curve of WASP-44b on 2012 October 13 using the U filter and subsequently on 2013 October 19 with the B and V filter (Tables 2, 11, 12, Fig. 6). The light-curve solution (Table 9) and planetary parameters (Table 14) are consistent with the discovery value and the error on the period is improved by a factor of 1.2 (Mancini et al. 2013). We also find a near-UV radius of $R_p/R_* = 0.1228 \pm 0.0028$, which is larger by 1.4σ with its optical radius of $R_p/R_* = 0.1164 \pm 0.0017$. An early near-UV or any non-spherical asymmetries are not observed in the data.

5.14 WASP-48b

WASP-48b is a typical inflated hot Jupiter orbiting a slightly evolved F star (Enoch et al. 2011). These parameters were confirmed by follow-up J -band primary transit observations by Sada et al. (2012). Secondary eclipse measurements indicate that WASP-48b has a weak temperature inversion and moderate day/night recirculation (O'Rourke et al. 2014). Ciceri et al. (2015) find that the spectrum of WASP-48b is flat from the optical to near-IR, which suggests that the atmosphere is not affected by large Rayleigh scattering. WASP-48 is the oldest system in our study with an age of $7.9^{+2.0}_{-1.6}$ Gyr and may have undergone synchronization of its stellar rotation with the planetary orbital period due to interactions with WASP-48b (Enoch et al. 2011).

We observed WASP-48b on 2012 October 9 using the U filter (Tables 2, 10, Fig. 6). The derived planetary parameters (Table 14) agree with the discovery values. We find a near-UV $R_p/R_* = 0.0916 \pm 0.0017$ which is 2.4σ smaller than its optical $R_p/R_* = 0.0980 \pm 0.0010$ (Enoch et al. 2011). We do not observe an early ingress in our near-UV transit.

5.15 WASP-77Ab

WASP-77Ab is a hot Jupiter orbiting a G8 star in a double-star system (Maxted et al. 2013). The host star exhibits moderate chromospheric activity determined by emission in the cores of the Ca II H & K lines and rotational modulation with a period of 15.3 d (Maxted et al. 2013). WASP-77 is the only multistar system in our sample where both companions are solar-like stars (G8 and K).

On 2012 December 06 using the U filter, we observed the first follow-up light curve of WASP-77Ab (Table 2, Fig. 7). The light-curve solution is in Table 12.

We make sure to correct for the dilution due to the companion star being in our aperture using the procedure described below. The separation of the stars are 3.3 arcsec (our seeing was 2.31–6.93 arcsec) and the magnitude differences between the components of the binary in the near-UV are $\Delta m_u = 2.961 \pm 0.015$ (Maxted et al. 2013). WASP-77Ab orbits around the brighter companion (WASP-77A). We perform the procedure described below to find the corrected R_p/R_* value and error. (1) We model the light curve with EXOMOP and find $(R_p/R_*)_{\text{uncor}} = 0.12612^{+0.00098}_{-0.00094}$ for the uncorrected case. (2) We then calculate the flux of WASP-77B (F_2) using the following equation:

$$m_1 - m_2 = \Delta m_u = 2.5 \log \left(\frac{F_1}{F_2} \right), \quad (16)$$

where m_1 is the magnitude of WASP-77A, m_2 is the magnitude of WASP-77B, F_2 is the flux measured in the aperture for WASP-77A (set equal to $1 \text{ erg s}^{-1} \text{ cm}^{-2} \text{ \AA}^{-1}$), and F_1 is the flux of

WASP-77B (found to be $0.065\,4034F_2$). (3) We then find the corrected $(R_p/R_*)_{\text{cor}}$ value using the equations

$$\left(\frac{R_p}{R_*}\right)_{\text{cor}} = \sqrt{\frac{\Delta F}{F_{\text{cor}}}} \quad (17)$$

$$\left(\frac{R_p}{R_*}\right)_{\text{cor}} = \sqrt{\frac{\Delta F}{F_2 - F_1}}, \quad (18)$$

where ΔF is the change in flux and is equal to $(R_p/R_*)_{\text{uncor}}^2$ and F_{cor} is the corrected flux for WASP-77A. (4) We propagate all the errors (including Δm_u and the error from EXOMOP modelling) to find the new error on the $(R_p/R_*)_{\text{cor}}$. Performing this procedure, we find a near-UV radius of $(R_p/R_*)_{\text{cor}} = 0.1305 \pm 0.0010$.

We agree with the discovery values for our planetary parameters and the error on the period is improved by a factor of 1.7 (Table 14). The near-UV radius of WASP-77Ab of $(R_p/R_*)_{\text{cor}} = 0.1305 \pm 0.0010$ is consistent with its optical $R_p/R_* = 0.130\,12 \pm 0.000\,65$ (Maxted et al. 2013).

6 DISCUSSION

6.1 Asymmetric transits

A large early ingress (Figs 1–7) or significant (>0.5 per cent) R_p/R_* difference (Tables 8–12) is not observed in any of our near-UV light curves. To investigate whether the transit shapes are symmetrical, we perform an asymmetry test where we subtract the mirror image of the transit with itself (see Section 3.1.3). Non-spherical asymmetries do not appear in any of these tests with the exception of WASP-33b, which is potentially the result of its host star’s variability (Herrero et al. 2011; Smith et al. 2011; Kovács et al. 2013). Therefore, within the precision (1.23–5.54 mmag) and timing resolution (61–137 s) of our observations no asymmetries are observed. Our results are consistent with the previous non-detections of an early ingress in the ground-based near-UV light curves of HAT-P-5b (Southworth et al. 2012b), HAT-P-16b (Pearson et al. 2014), TrES-3b (Turner et al. 2013), WASP-12b (Copperwheat et al. 2013), WASP-17b (Bento et al. 2014), and XO-2b (Zellem et al. 2015).

Additionally, the non-detection of asymmetrical transits confirms and expands upon the theoretical modelling done by Ben-Jaffel & Ballester (2014) and Turner et al. (2016). These theoretical studies concentrated on modelling the corona around solar-like stars. Therefore, since the targets in this study are deliberately chosen to have a variety of planetary and host star parameters (Table 1), based on the work in this paper we do not expect to observe near-UV asymmetries caused by an opacity source in the stellar corona in any system regardless of its spectral type.

6.1.1 Variability in the bow shock

Assuming that the bow shock is sufficiently optically thick to absorb light from the host star during transit, then we need to assess whether shock variability is a key factor in the non-detections. It is predicted that bow shock variations would be common for planets that are not circularized, not in the corotation radius of their host star, and orbiting around active stars (Vidotto et al. 2011a; Llama et al. 2013). Rossiter–McLaughlin effect (McLaughlin 1924; Rossiter 1924; Winn 2011) measurements and activity indicators can assess whether any of the systems would be prone to bow shock variability.

Measurements of the Rossiter–McLaughlin effect can be used to determine whether our systems are coplanar with their hosts stars. If the coronal material is axisymmetric and if a planet’s orbital plane and the stellar equator are coplanar then the planet will move through coronal material of constant density and temperature during transit. In our sample, we have four planets (CoRoT-1b, WASP-1b, WASP-12b, WASP-33b) that are not aligned with their stars, five planets (HAT-P-1b, HAT-P-13b, HAT-P-16b, TrES-2b, TrES-4b) that are aligned with their stars, and six planets (GJ 436b, HAT-P-22b, WASP-36b, WASP-44b, WASP-48b, WASP-77Ab) that are in need of Rossiter–McLaughlin measurements (See Table 1). Therefore, it is possible that members of our sample may exhibit shock variability due to the planet moving through coronal material with different densities. However, this phenomenon does not explain all our non-detections since the planets that are aligned with their host stars are moving through coronal material with a similar density and through an environment with a constant stellar magnetic field.

Furthermore, if the host stars are active then fluctuations in the stellar wind, flaring, or coronal mass ejections could cause inhomogeneity in the coronal outflow. The R'_{HK} index, the ratio between chromospheric activity to the total bolometric emission of the star, can be used to gauge the amount of stellar activity of a star (Noyes et al. 1984) and more active stars exhibit higher R'_{HK} indices. In our sample, there are six planets (CoRoT-1b, GJ436b, HAT-P-13b, TrES-4b, WASP-1b, WASP-12b) with a R'_{HK} index lower than the sun ($R'_{\text{HK},\odot} = -4.96$), 1 planet (HAT-P-16b) with a $R'_{\text{HK}} > R'_{\text{HK},\odot}$, two planets (HAT-P-1b, TrES-2b) with a $R'_{\text{HK}} \sim R'_{\text{HK},\odot}$, and six planets (HAT-P-22b, WASP-33b, WASP-36b, WASP-44b, WASP-48b, WASP-77Ab) that do not have a R'_{HK} index measured (Table 1). Therefore, some of the non-detections of the planets around the active stars could be caused by their orbits moving through inhomogeneous coronal material. Also, stellar flares can raise the coronal temperature above the maximum temperature allowed for shock formation (VJH11a). HAT-P-16b (the only planet in our sample known to orbit an active host star) is observed more than once and all the observations result in non-detections despite six months between successive observations. Additionally, WASP-12b, WASP-1b, and GJ436b (planets known to orbit non-active host stars) are observed more than once and also result in non-detections. Therefore, variability of the coronal plasma may be causing some of our non-detections but not all of them.

However, the interpretation of variability causing some of our non-detections changes significantly if we now consider the theoretical study by Turner et al. (2016). Turner et al. (2016) did an extensive parameter study to determine if temperature ($3 \times 10^4 - 2 \times 10^6$ K) or density ($10^4 - 10^8$ cm $^{-3}$) changes in the coronal outflow would cause variation in the absorption due to the bow shock. They find that under all reasonable conditions for a steady state and varying stellar corona that no absorption occurred in the bow shock. Therefore, we did not observe any asymmetries in our observations because the bow shock does not actually cause any absorption in the first place and not due to bow shock variability.

6.2 Wavelength dependence on the planetary radius

Observing the primary transit of an exoplanet at multiple wavelengths allows for an investigation into the composition and structure of its atmosphere. The measured R_p/R_* depends on the opacity of the planetary atmosphere and thus allows for useful insights into the atmosphere’s spectral features and composition. If the opacity in our near-UV band is dominated by Rayleigh scattering of

molecular hydrogen, it may be possible to place strong upper limits on the planet's 10 bar radius (Tinetti et al. 2010; Benneke & Seager 2012; Benneke & Seager 2013; Griffith 2014). Such constraints can break the degeneracy between an exoplanet's physical radius and atmospheric composition in radiative transfer retrievals (e.g. Lecavelier Des Etangs et al. 2008; Tinetti et al. 2010; Benneke & Seager 2012; Griffith 2014).

The R_p/R_* of 10 exoplanets (GJ436b, HAT-P-1b, HAT-P-13b, HAT-P-16b, HAT-P-22b, TrES-2b, WASP-33b, WASP-44b, WASP-48b, WASP-77Ab) are consistent to within 1σ of their optical R_p/R_* (Tables 13–14). Clouds in the upper atmospheres of these planets are consistent with these observations because clouds reduce the strengths of spectral features (e.g. Seager & Sasselov 2000; Brown 2001; Gibson et al. 2013b; Kreidberg et al. 2014). Also, day-side spectral features may be absent due to an isothermal pressure-temperature profile (Fortney et al. 2006). These planets are consistent with other transiting exoplanet observations with flat spectra in optical wavelengths on TrES-3b (Turner et al. 2013), GJ 3470b (a hot Uranus; Biddle et al. 2014), GJ 1214b (Bean et al. 2011; Kreidberg et al. 2014), WASP-29b (Gibson et al. 2013a), and HAT-P-32b (Gibson et al. 2013b).

We also find that some of our targets do not exhibit a flat spectrum. The R_p/R_* of CoRoT-1b, TrES-4b, and WASP-12b are larger than their optical R_p/R_* by 2.3σ , 2σ , and 2.5σ , respectively (Tables 13 and 14). This variation corresponds to a difference in the radius of 6 scaleheights (H) for both CoRoT-1b and TrES-4b and 3H for WASP-12b. This is consistent with the 6H variation observed in HD 189733b (Sing et al. 2011). A larger near-UV radius may indicate non-uniform clouds (Griffith 2014) or Rayleigh scattering in their atmospheres (Tinetti et al. 2010; Benneke & Seager 2012; Benneke & Seager 2013; Griffith 2014). Additionally, the near-UV R_p/R_* of WASP-1b and WASP-36b are smaller than their optical R_p/R_* by 3.6σ and 2.6σ (Tables 13 and 14), respectively. To our knowledge, this is the first time a hot Jupiter has been observed to have a smaller near-UV transit depth than that measured in the optical. Additionally, the near-UV transit depths of WASP-1b and WASP-36b are smaller than every transit depth measurement made on the planets (Table 16). More work is needed to investigate possible opacity sources that can cause such a transit depth variation. The variation corresponds to a difference of 7 and 20H for WASP-1b and WASP-36b, respectively. The large scaleheight variations are similar with the 13H variation found for WASP-103b (Southworth et al. 2015). These results are consistent with other exoplanets not having flat spectrum (HD 209458b, Sing et al. 2008; HAT-P-5b, Southworth et al. 2012b; GJ 3470b, Nascimbeni et al. 2013; Qatar-2, Mancini et al. 2014).

For illustration, we compare the observed R_p/R_* differences with wavelength for each target (Table 16) to theoretical predictions by Fortney et al. (2010) for a model planetary atmosphere (Figs 8–10). The models used were estimated for planets with a $1 M_{\text{Jup}}$, $g_p = 25 \text{ m s}^{-1}$, base radius of $1.25 R_{\text{Jup}}$ at 10 bar, solar metallicity,

and T_{eq} closest to the measured value for each exoplanet (with model choices of 500, 750, 1000, 1250, 1500, 1750, 2000, 2500 K). Additionally, TiO and VO opacity were not included in the synthetic model. A vertical offset was applied to the model to provide the best fit to the spectral changes. This comparison is useful as it is illustrative of the size of variation of the observations compared to what the models predict. However, in-depth radiative transfer models calculated for all the exoplanets are still needed to fully understand their transmission spectra.

Next, we apply the MassSpec concept (Lecavelier Des Etangs et al. 2008, de Wit & Seager 2013) to the spectral slope to determine if the observed radius variations are consistent with Rayleigh scattering. This approximation assumes a well mixed, isothermal atmosphere in chemical equilibrium, and an effective atmospheric opacity source with an extinction cross-section which follows a power-law index, α , $\sigma = \sigma_0(\lambda/\lambda_0)^\alpha$. The slope of the spectrum is related to α by using the scaleheight (Lecavelier Des Etangs et al. 2008)

$$\alpha H = \frac{dR_b(\lambda)}{d \ln \lambda}, \quad (19)$$

where λ is the wavelength. An $\alpha = -4$ would be consistent with Rayleigh scattering (Lecavelier Des Etangs et al. 2008). In order to calculate α , we use our near-UV R_p/R_* values and the literature values of the nearest wavelength (Table 16). In some cases, the nearest literature wavelength are not in the blue part of the spectra. This lack of measurement can cause a problem in the interpretation of α because the U and B bands are the only bands where strong spectral features are not present (Tinetti et al. 2010; Benneke & Seager 2012; Benneke & Seager 2013; Griffith 2014). The calculation of α also assumes that only a single species is dominant in the atmosphere, an assumption that may not always hold. We find an α of -17.3 ± 7.9 , -19.1 ± 2.4 , and -5.9 ± 0.9 for CoRoT-1b, TrES-4b, and WASP-12b, respectively. The spectral index calculated for WASP-12b (see also Sing et al. 2013) and CoRoT-1b are within 2σ of Rayleigh scattering. Follow-up observations are needed to confirm this result. Additionally, an α of $+11.6 \pm 1.1$ and $+34.8 \pm 2.7$ are found for WASP-1b and WASP-36b, respectively. This is the first time a positive α has been estimated for any exoplanet and more theoretical modelling is needed to identify possible opacity sources.

6.2.1 Variability due to the host stars

Our interpretation that the observed wavelength variations are due to the planetary atmosphere assumes that the host stars do not vary significantly due to stellar activity. The presence of stellar activity and star-spots on the stellar surface can produce variations in the observed transit depth when measured at different times (e.g. Czesla et al. 2009; Oshagh et al. 2013; Oshagh et al. 2014; Zellem et al.

Table 16. R_p/R_* and central wavelength λ_{eff} from this paper and previous literature for all targets.^a

Planet	Source	Filter	Wavelength (nm)	R_p/R_*
CoRoT-1b	This Paper	Bessell U	370	$0.1439^{+0.0020}_{-0.0018}$
CoRoT-1b	Gillon et al. (2009)	R SPECIAL	655	0.1381 ± 0.0007
CoRoT-1b	Schlawin et al. (2014)	IRTF	860	0.1470 ± 0.0020

^aThis table is available in its entirety in machine-readable form in the online journal. A portion is shown here for guidance regarding its form and content.

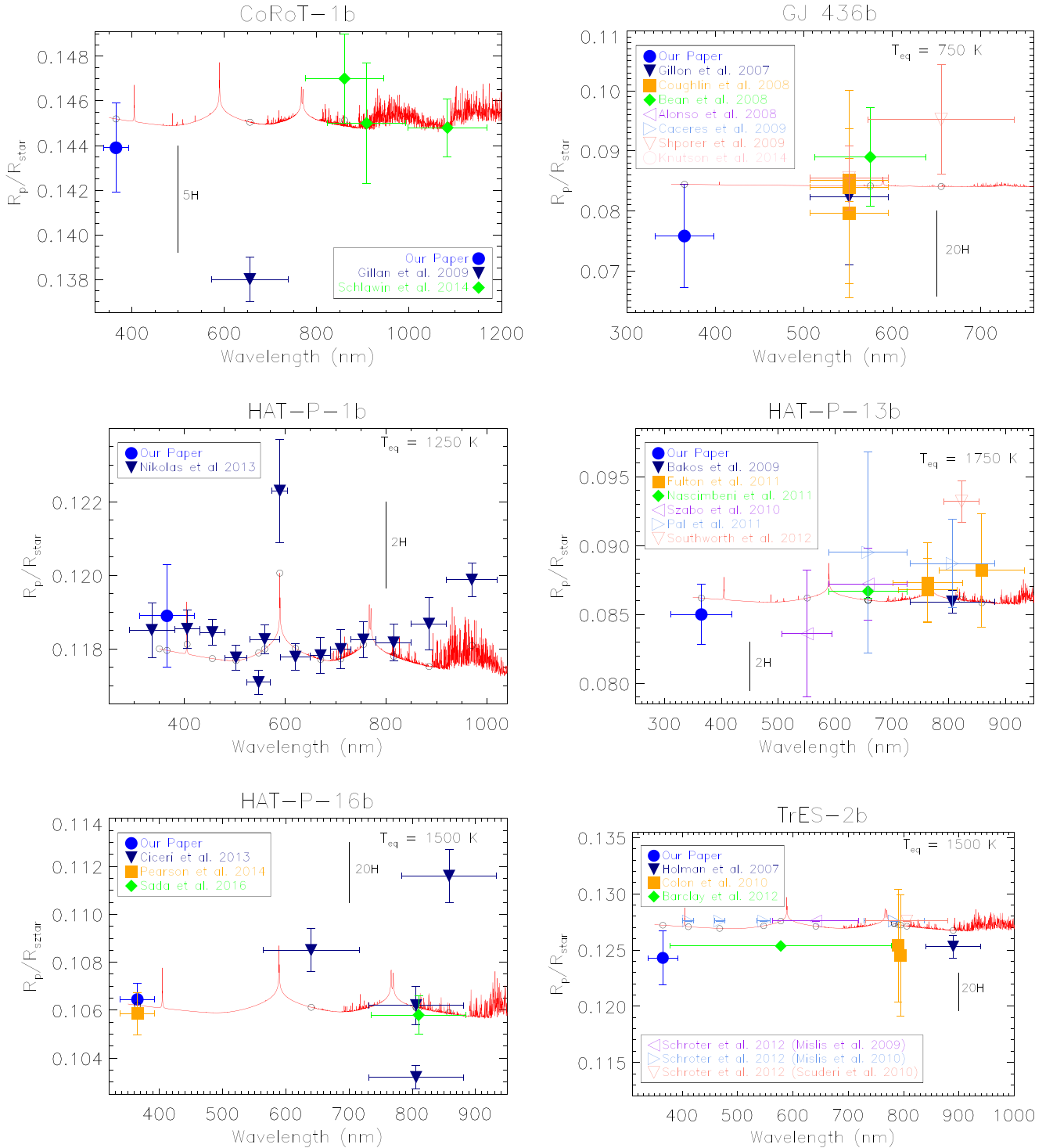


Figure 8. Variation of R_p/R_* versus wavelength for CoRoT-1b, GJ 436b, HAT-P-1b, HAT-P-13b, HAT-P-16b, and TrES-2b. Overplotted in red are atmospheric models by Fortney et al. (2010) for planets with a $1 M_{\text{Jup}}$, $g_p = 25 \text{ m s}^{-1}$, base radius of $1.25 R_{\text{Jup}}$ at 10 bar, and T_{eq} (specified on plot). The scaleheight of the planet is also shown on each plot for reference.

2015). This effect is particularly stronger in the near-UV than in the optical and can mimic a Rayleigh scattering signature (e.g. Oshagh et al. 2014; McCullough et al. 2014). As described in Section 6.1.1, for the planets with measured R'_{HK} indices only one (HAT-P-16b) in our sample is known to orbit an active star (Table 1). Additionally, no obvious star-spot crossing is seen in our data (Figs 1–5). The WASP-1b and WASP-36b near-UV and optical observations were

done at the same time, thus the influence of stellar activity on the smaller near-UV transit depth result should be minimal.

Next, we estimate how much the transit depth changes due to unocculted spots using the formalization presented by Sing et al. (2011). The three main assumptions of this method are that the emission spectrum of the spots are treated as a stellar spectrum but with a lower effective temperature, the surface brightness outside the

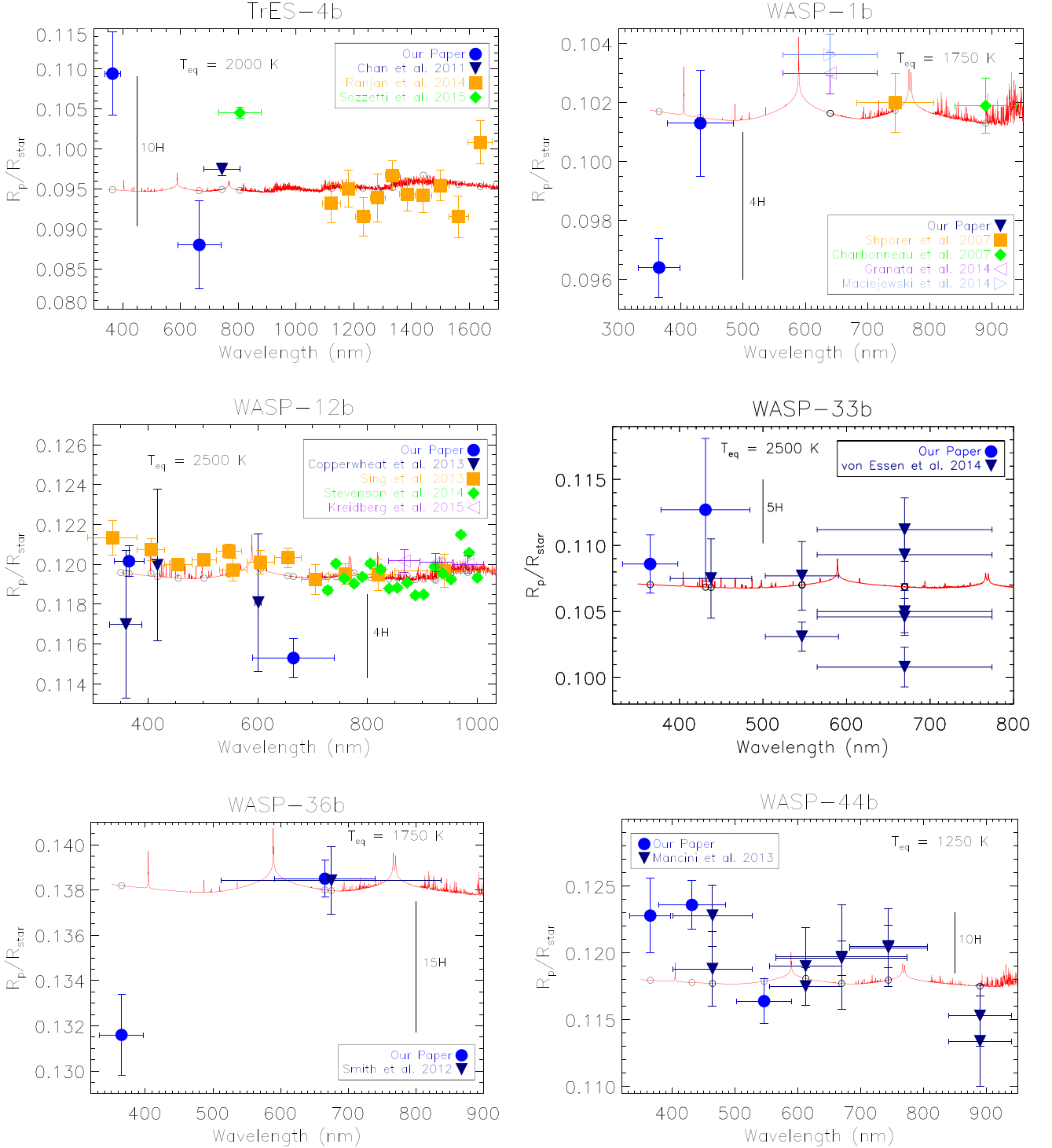


Figure 9. Variation of R_p/R_* versus wavelength for TrES-4b, WASP-1b, WASP-12b, WASP-33b, WASP-36, and WASP-44b. The observation of a smaller near-UV than the optical radius on WASP-1b and WASP-36b are the first of such a detection on a hot Jupiter. Other comments are the same as Fig. 8.

spots does not change, and no facule are present. These assumptions lead to an overall dimming of the star and increase in the transit depth. Sing et al. (2011) find that the change in transit depth due to unocculted spots, $\Delta(R_p/R_*)$, is

$$\Delta \left(\frac{R_p}{R_*} \right) = \frac{1}{2} \frac{\Delta d}{d} \frac{R_p}{R_*}, \quad (20)$$

where

$$\frac{\Delta d}{d} = \Delta f(\lambda_0, t) \left(1 - \frac{F_{\lambda}^{T_{\text{spot}}}}{F_{\lambda}^{T_{\text{star}}}} \right) / \left(1 - \frac{F_{\lambda_0}^{T_{\text{spot}}}}{F_{\lambda_0}^{T_{\text{star}}}} \right), \quad (21)$$

$\Delta f(\lambda_0, t)$ is the total dimming at the reference wavelength (λ_0) over some time-scale (t), and F_{λ}^T is the surface brightness of the stellar models at the temperature of the star (T_{star}) and the spot (T_{spot}). An exact value for $\Delta(R_p/R_*)$ is beyond that scope of this paper since

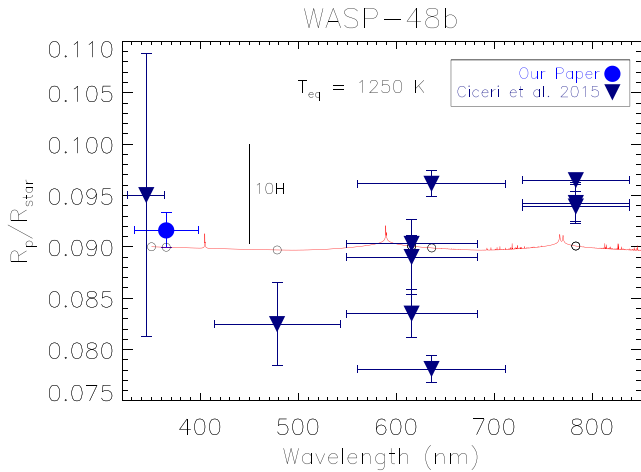


Figure 10. Variation of R_p/R_* versus wavelength for WASP-48b. Other comments are the same as Fig. 8.

the $\Delta f(\lambda_0, t)$ and T_{spot} are unknown for all targets. Sing et al. (2011) find for HD 189733b that $\Delta(R_p/R_*) = 2.08 \times 10^{-3}/2 (R_p/R_*)$ between 375 and 400 nm assuming $T_{\text{spot}} = 4250$ K, $T_{\text{star}} = 5000$ K, $\Delta f(\lambda_0) = 1$ per cent, and $\lambda_0 = 400$ nm. Therefore, unocculted spots have minimal influence (assuming the stars we are observing have spots similar to HD 189733b) on the observed transit depth variations since the influence of these spots are about 10 times smaller (e.g. $\Delta[R_p/R_*] = 0.00014$ for WASP-36b) than our final error bars (Tables 13 and 14). This result is also consistent with the recent study by Llama & Shkolnik (2015) that find that stellar activity similar to that of the sun has minimal effect on the transit depth in the wavelengths explored in our study. None the less, follow-up observations and host star monitoring are encouraged to monitor the effect of stellar activity on the transit depth variations we observe.

7 CONCLUSIONS

We investigate the primary transits of the 15 exoplanets (CoRoT-1b, GJ436b, HAT-P-1b, HAT-P-13b, HAT-P-16b, HAT-P-22b, TrES-2b, TrES-4b, WASP-1b, WASP-12b, WASP-33b, WASP-36b, WASP-44b, WASP-48b, WASP-77Ab) using ground-based near-UV and optical filters to study their atmospheres (Section 6.2; Figs 8–10; Table 16). A constant R_p/R_* from near-UV to optical wavelengths is found for 10 targets (GJ436b, HAT-P-1b, HAT-P-13b, HAT-P-16b, HAT-P-22b, TrES-2b, WASP-33b, WASP-44b, WASP-48b, WASP-77Ab), suggestive of clouds in their atmospheres. Additionally, the near-UV R_p/R_* of 3 targets (CoRoT-1b, TrES-4b, WASP-12b) are larger and 2 targets (WASP-1b, WASP-36b) are smaller by at least 2σ from their optical R_p/R_* . The atmospheric implications of the transit depth variations are explored (Section 6.2) and we find that the spectral slope of WASP-12b and CoRoT-1b are consistent with Rayleigh scattering. To our knowledge, this is the first time a hot Jupiter has been observed to have a smaller near-UV transit depth than optical and a possible opacity source that can cause such a radius variation is currently unknown. The WASP-1b and WASP-36b near-UV and optical observations were done at the same time, thus limiting the influence of stellar activity on the transit depth variations. Follow-up observations are encouraged to confirm all our results but especially the observation of a smaller near-UV transit depth.

Additionally, we do not detect any near-UV light-curve asymmetries in all of the 15 targets within the precision (1.23–6.22

mmag) and timing resolution (27–137 s) of our observations (Table 2, Section 6.1). All the non-detections in this study confirm and expand upon the theoretical modelling done by Ben-Jaffel & Ballester (2014) and Turner et al. (2016) that near-UV asymmetries cannot be seen from the ground. These findings are consistent with the previous ground-based non-detection of asymmetries in HAT-P-16b (Pearson et al. 2014) and WASP-12b (Copperwheat et al. 2013) and four (HAT-P-5b, TrES-3b, WASP-17b, XO-2b) other exoplanets (Southworth et al. 2012b; Turner et al. 2013; Bento et al. 2014; Zellem et al. 2015).

Finally, for each target we derive a new set of planetary system parameters and the orbital period and ephemeris are updated to help with follow-up observations (Tables 13 and 14). Our data includes the first published ground-based near-UV light curves of 12 of the targets (CoRoT-1b, GJ436b, HAT-P-1b, HAT-P-13b, HAT-P-22b, TrES-2b, TrES-4b, WASP-1b, WASP-33b, WASP-36b, WASP-48b, WASP-77Ab) and greatly expands the number of near-UV light curves in the literature.

ACKNOWLEDGEMENTS

JDT, KAP, RTZ, JKT, and CCG were partially supported by the NASA's Planetary Atmospheres programme. JDT was also partially funded by the Virginia Space Grant Consortium Graduate Research Fellowship Program and by the National Science Foundation Graduate Research Fellowship under Grant no. DGE-1315231.

We sincerely thank the University of Arizona Astronomy Club, the Steward Observatory TAC, the Steward Observatory telescope day crew, John Biegging, Elizabeth Green, Don McCarthy, Maria Schuchardt, the Lunar and Planetary Laboratory, and the Associated Students of the University of Arizona for supporting this research.

We also thank John Southworth, Jason Eastman, Ian Crossfield, Josh Carter, and John Johnson for their helpful comments on JKTEBOP, EXOFAST, TAP, and EXOMOP. We also thank Joe Llama for the discussion on his bow shock models and Aline Vidotto, Moira Jardine, and Christiane Helling on the useful discussion of their UV bow shock predictions. Finally, we would like to thank Michael Cushing, Jon Bjorkman, Robert Johnson, Carl Schmidt, Phil Arras, and Andrew Collier Cameron for their insightful comments on this research.

This research has made use of the Exoplanet Orbit Database (Wright et al. 2011), Exoplanet Data Explorer at exoplanets.org, Exoplanet Transit Database, Extrasolar Planet Transit Finder, NASA's Astrophysics Data System Bibliographic Services, and the International Variable Star Index (VSX) data base, operated at AAVSO, Cambridge, Massachusetts, USA.

We would also like to thank the anonymous referee for their insightful comments during the publication process. This manuscript is much improved thanks to their comments.

NOTE ADDED IN PROOF

After this paper was accepted, Evans et al. (2016) presented observations of WASP-121b and find that their transit depths in the optical (B and r' bands) are much deeper relative to the near-infrared wavelengths. They interpret this result as being caused by TiO and VO absorption and this might also be the cause of the transit depth variations we find for WASP-1b and WASP-36b.

REFERENCES

- Albrecht S. et al., 2011, *ApJ*, 738, 50
- Albrecht S. et al., 2012, *ApJ*, 757, 18

- Alonso R., Barbieri M., Rabus M., Deeg H. J., Belmonte J. A., Almenara J. M., 2008, *A&A*, 487, L5
- Alonso R. et al., 2009, *A&A*, 506, 353
- Anderson D. R. et al., 2012, *MNRAS*, 422, 1988
- Aschwanden M. J., 2005, *Physics of the Solar Corona, An Introduction with Problems and Solutions* (2nd edition). Springer, Berlin
- Baglin A., 2003, *Adv. Space Res.*, 31, 345
- Bakos G. Á., Lázár J., Papp I., Sári P., Green E. M., 2002, *PASP*, 114, 974
- Bakos G. Á. et al., 2007, *ApJ*, 656, 552
- Bakos G. Á. et al., 2009, *ApJ*, 707, 446
- Bakos G. Á. et al., 2011, *ApJ*, 742, 116
- Ballard S. et al., 2010, *PASP*, 122, 1341
- Ballerini P., Micela G., Lanza A. F., Pagano I., 2012, *A&A*, 539, A140
- Barclay T. et al., 2012, *ApJ*, 761, 53
- Barge P. et al., 2008, *A&A*, 482, L17
- Barnes J. W., van Eyken J. C., Jackson B. K., Ciardi D. R., Fortney J. J., 2013, *ApJ*, 774, 53
- Bean J. L., 2009, *A&A*, 506, 369
- Bean J. L., Seifahrt A., 2008, *A&A*, 487, L25
- Bean J. L., Benedict G. F., Endl M., 2006, *ApJ*, 653, L65
- Bean J. L. et al., 2008, *A&A*, 486, 1039
- Bean J. L. et al., 2011, *ApJ*, 743, 92
- Bechter E. B. et al., 2014, *ApJ*, 788, 2
- Béky B., Holman M. J., Gilliland R. L., Bakos G. Á., Winn J. N., Noyes R. W., Sasselov D. D., 2013, *AJ*, 145, 166
- Ben-Jaffel L., 2007, *ApJ*, 671, L61
- Ben-Jaffel L., 2008, *ApJ*, 688, 1352
- Ben-Jaffel L., Ballester G. E., 2013, *A&A*, 553, A52
- Ben-Jaffel L., Ballester G. E., 2014, *ApJ*, 785, L30
- Benneke B., Seager S., 2012, *ApJ*, 753, 100
- Benneke B., Seager S., 2013, *ApJ*, 778, 153
- Bento J. et al., 2014, *MNRAS*, 437, 1511
- Bergfors C. et al., 2013, *MNRAS*, 428, 182
- Biddle L. I. et al., 2014, *MNRAS*, 443, 1810
- Bonnarel F. et al., 2000, *A&AS*, 143, 33
- Braak C., 2006, *Stat. Comput.*, 16, 239
- Brown T. M., 2001, *ApJ*, 553, 1006
- Bruntt H., Southworth J., Torres G., Penny A. J., Clausen J. V., Buzasi D. L., 2006, *A&A*, 456, 651
- Buchhave L. A. et al., 2010, *ApJ*, 720, 1118
- Burton J. R., Watson C. A., Rodríguez-Gil P., Skillen I., Littlefair S. P., Dhillion S., Pollacco D., 2015, *MNRAS*, 446, 1071
- Butler R. P., Vogt S. S., Marcy G. W., Fischer D. A., Wright J. T., Henry G. W., Laughlin G., Lissauer J. J., 2004, *ApJ*, 617, 580
- Cabrera J. et al., 2015, *A&A*, 579, A36
- Cáceres C., Ivanov V. D., Minniti D., Naef D., Melo C., Mason E., Selman F., Pietrzynski G., 2009, *A&A*, 507, 481
- Campo C. J. et al., 2011, *ApJ*, 727, 125
- Carter J. A., Winn J. N., 2009, *ApJ*, 704, 51
- Carter J. A., Yee J. C., Eastman J., Gaudi B. S., Winn J. N., 2008, *ApJ*, 689, 499
- Cauley P. W., Redfield S., Jensen A. G., Barman T., Endl M., Cochran W. D., 2015, *ApJ*, 810, 13
- Chan T., Ingemymr M., Winn J. N., Holman M. J., Sanchis-Ojeda R., Esquerdo G., Everett M., 2011, *AJ*, 141, 179
- Charbonneau D., Winn J. N., Everett M. E., Latham D. W., Holman M. J., Esquerdo G. A., O'Donovan F. T., 2007, *ApJ*, 658, 1322
- Christiansen J. L. et al., 2011, *ApJ*, 726, 94
- Ciceri S. et al., 2013, *A&A*, 557, A30
- Ciceri S. et al., 2015, *A&A*, 577, A54
- Claret A., Bloemen S., 2011, *A&A*, 529, A75
- Collier Cameron A. et al., 2007, *MNRAS*, 375, 951
- Collier Cameron A. et al., 2010, *MNRAS*, 407, 507
- Collins K. A., Kielkopf J. F., Stassun K. G., 2015, preprint ([arXiv:1512.00464](https://arxiv.org/abs/1512.00464))
- Colón K. D., Ford E. B., Lee B., Mahadevan S., Blake C. H., 2010, *MNRAS*, 408, 1494
- Copperwheat C. M. et al., 2013, *MNRAS*, 434, 661
- Coughlin J. L., Stringfellow G. S., Becker A. C., López-Morales M., Mezzalana F., Kraljić T., 2008, *ApJ*, 689, L149
- Cowan N. B., Machalek P., Croll B., Shekhtman L. M., Burrows A., Deming D., Greene T., Hora J. L., 2012, *ApJ*, 747, 82
- Croll B., Albert L., Lafreniere D., Jayawardhana R., Fortney J. J., 2010, *ApJ*, 717, 1084
- Croll B., Lafreniere D., Albert L., Jayawardhana R., Fortney J. J., Murray N., 2011, *AJ*, 141, 30
- Croll B. et al., 2015, *ApJ*, 802, 28
- Crossfield I. J. M., Hansen B. M. S., Barman T., 2012, *ApJ*, 746, 46
- Crossfield I. J. M., Barman T., Hansen B. M. S., Howard A. W., 2013, *A&A*, 559, A33
- Csizmadia S. et al., 2010, *A&A*, 510, A94
- Czesla S., Huber K. F., Wolter U., Schröter S., Schmitt J. H. M. M., 2009, *A&A*, 505, 1277
- de Mooij E. J. W., Brogi M., de Kok R. J., Snellen I. A. G., Kenworthy M. A., Karjalainen R., 2013, *A&A*, 550, A54
- de Wit J., Seager S., 2013, *Science*, 342, 1473
- Deming D., Harrington J., Laughlin G., Seager S., Navarro S. B., Bowman W. C., Horning K., 2007, *ApJ*, 667, L199
- Deming D. et al., 2011, *ApJ*, 726, 95
- Deming D. et al., 2012, *ApJ*, 754, 106
- Demory B.-O. et al., 2007, *A&A*, 475, 1125
- Demory B.-O. et al., 2013, *ApJ*, 776, L25
- Dittmann J. A., Close L. M., Green E. M., Scuderi L. J., Males J. R., 2009a, *ApJ*, 699, L48
- Dittmann J. A., Close L. M., Green E. M., Fenwick M., 2009b, *ApJ*, 701, 756
- Dittmann J. A., Close L. M., Scuderi L. J., Morris M. D., 2010, *ApJ*, 717, 235
- Dittmann J. A., Close L. M., Scuderi L. J., Turner J., Stephenson P. C., 2012, *New Astron.*, 17, 438
- Eastman J., Siverd R., Gaudi B. S., 2010, *PASP*, 122, 935
- Eastman J., Gaudi B. S., Agol E., 2013, *PASP*, 125, 83
- Ehrenreich D., Lecavelier Des Etangs A., Delfosse X., 2011, *A&A*, 529, A80
- Ehrenreich D. et al., 2012, *A&A*, 547, A18
- Ehrenreich D. et al., 2015, *Nature*, 522, 459
- Enoch B. et al., 2011, *AJ*, 142, 86
- Esteves L. J., De Mooij E. J. W., Jayawardhana R., 2013, *ApJ*, 772, 51
- Evans T. M. et al., 2016, preprint ([ArXiv:1604.02310](https://arxiv.org/abs/1604.02310))
- Ferland G. J., Korista K. T., Verner D. A., Ferguson J. W., Kingdon J. B., Verner E. M., 1998, *PASP*, 110, 761
- Ferland G. J. et al., 2013, *Rev. Mex. Astron. Astrofis*, 49, 137
- Figueira P., Pont F., Mordasini C., Alibert Y., Georgy C., Benz W., 2009, *A&A*, 493, 671
- Föhring D., Dhillion V. S., Madhusudhan N., Marsh T. R., Copperwheat C. M., Littlefair S. P., Wilson R. W., 2013, *MNRAS*, 435, 2268
- Ford E. B., 2006, *ApJ*, 642, 505
- Fortney J. J., Cooper C. S., Showman A. P., Marley M. S., Freedman R. S., 2006, *ApJ*, 652, 746
- Fortney J. J., Lodders K., Marley M. S., Freedman R. S., 2008, *ApJ*, 678, 1419
- Fortney J. J., Shabram M., Showman A. P., Lian Y., Freedman R. S., Marley M. S., Lewis N. K., 2010, *ApJ*, 709, 1396
- Fossati L. et al., 2010, *ApJ*, 714, L222
- Fossati L., Ayres T. R., Haswell C. A., Bohlender D., Kochukhov O., Flöer L., 2013, *ApJ*, 766, L20
- Fossati L. et al., 2015, preprint ([arXiv:1503.01278](https://arxiv.org/abs/1503.01278))
- Fulton B. J., Shporer A., Winn J. N., Holman M. J., Pál A., Gazak J. Z., 2011, *AJ*, 142, 84
- Gaidos E. et al., 2014, *MNRAS*, 437, 3133
- Gazak J. Z., Johnson J. A., Tonry J., Dragomir D., Eastman J., Mann A. W., Agol E., 2012, *Adv. Astron.*, 697, 967
- Gelman A., Rubin D. B., 1992, *Stat. Sci.*, 7, 457
- Gibson N. P. et al., 2010, *MNRAS*, 404, L114
- Gibson N. P., Aigrain S., Barstow J. K., Evans T. M., Fletcher L. N., Irwin P. G. J., 2013a, *MNRAS*, 428, 3680

- Gibson N. P., Aigrain S., Barstow J. K., Evans T. M., Fletcher L. N., Irwin P. G. J., 2013b, *MNRAS*, 436, 2974
- Gilliland R. L. et al., 2010, *ApJ*, 713, L160
- Gillon M. et al., 2007a, *A&A*, 471, L51
- Gillon M. et al., 2007b, *A&A*, 472, L13
- Gillon M. et al., 2009, *A&A*, 506, 359
- Granata V., Nascimbeni V., Piotto G., Bedin L. R., Borsato L., Cunial A., Damasso M., Malavolta L., 2014, *Astron. Nachr.*, 335, 797
- Griffith C. A., 2014, *Phil. Trans. R. Soc. A*, 372, 30086
- Hansen B. M. S., Barman T., 2007, *ApJ*, 671, 861
- Hardy L. K., Butterley T., Dhillon V. S., Littlefair S. P., Wilson R. W., 2015, *MNRAS*, 454, 4316
- Haswell C. A. et al., 2012, *ApJ*, 760, 79
- Haynes K., Mandell A. M., Madhusudhan N., Deming D., Knutson H., 2015, *ApJ*, 806, 146
- Hebb L. et al., 2009, *ApJ*, 693, 1920
- Herrero E., Morales J. C., Ribas I., Naves R., 2011, *A&A*, 526, L10
- Holman M. J. et al., 2007, *ApJ*, 664, 1185
- Howard A. W. et al., 2013, *Nature*, 503, 381
- Hoyer S., Rojo P., López-Morales M., Díaz R. F., Chambers J., Minniti D., 2011, *ApJ*, 733, 53
- Hoyer S., Rojo P., López-Morales M., 2012, *ApJ*, 748, 22
- Husnoo N. et al., 2011, *MNRAS*, 413, 2500
- Husnoo N., Pont F., Mazeh T., Fabrycky D., Hébrard G., Bouchy F., Shporer A., 2012, *MNRAS*, 422, 3151
- Jenkins J. M., Caldwell D. A., Borucki W. J., 2002, *ApJ*, 564, 495
- Johnson J. A. et al., 2008, *ApJ*, 686, 649
- Johnson M. C., Cochran W. D., Collier Cameron A., Bayliss D., 2015, *ApJ*, 810, L23
- Kipping D., Bakos G., 2011, *ApJ*, 733, 36
- Kipping D. M., Spiegel D. S., 2011, *MNRAS*, 417, L88
- Kipping D. M. et al., 2010, *ApJ*, 725, 2017
- Kislyakova K. G. et al., 2013, *Astrobio*, 13, 1030
- Knutson H. A., Howard A. W., Isaacson H., 2010, *ApJ*, 720, 1569
- Knutson H. A. et al., 2011, *ApJ*, 735, 27
- Knutson H. A. et al., 2014, *ApJ*, 785, 126
- Knutson H. A., Benneke B., Deming D., Homeier D., 2014, *Nature*, 505, 66
- Kovács G. et al., 2013, *A&A*, 553, A44
- Kreidberg L. et al., 2014, *Nature*, 505, 69
- Kreidberg L. et al., 2015, *ApJ*, 814, 66
- Kulow J. R., France K., Linsky J., Loyd R. O. P., 2014, *ApJ*, 786, 132
- Lai D., Helling C., van den Heuvel E. P. J., 2010, *ApJ*, 721, 923
- Lanotte A. A. et al., 2014, *A&A*, 572, A73
- Lecavelier Des Etangs A., Vidal-Madjar A., Désert J.-M., Sing D., 2008, *A&A*, 485, 865
- Line M. R., Knutson H., Wolf A. S., Yung Y. L., 2014, *ApJ*, 783, 70
- Liu F., Asplund M., Ramírez I., Yong D., Meléndez J., 2014, *MNRAS*, 442, L51
- Llama J., Shkolnik E. L., 2015, *ApJ*, 802, 41
- Llama J., Wood K., Jardine M., Vidotto A. A., Helling C., Fossati L., Haswell C. A., 2011, *MNRAS*, 416, L41
- Llama J., Vidotto A. A., Jardine M., Wood K., Fares R., Gombosi T. I., 2013, *MNRAS*, 436, 2179
- López-Morales M., Coughlin J. L., Sing D. K., Burrows A., Apai D., Rogers J. C., Spiegel D. S., Adams E. R., 2010, *ApJ*, 716, L36
- McCullough P. R., Crouzet N., Deming D., Madhusudhan N., 2014, *ApJ*, 791, 55
- Maceroni C., Rucinski S. M., 1997, *PASP*, 109, 782
- Maciejewski G., Ermann R., Raetz S., Seeliger M., Spaleniak I., Neuhauser R., 2011, *A&A*, 528, A65
- Maciejewski G. et al., 2013, *A&A*, 551, A108
- Maciejewski G. et al., 2014, *Acta Astron.*, 64, 27
- Maciejewski G. et al., 2016, preprint ([arXiv:1603.03268](https://arxiv.org/abs/1603.03268))
- McKenzie J. F., Axford W. I., Banaszkiewicz M., 1997, *Geophys. Res. Lett.*, 24, 2877
- McLaughlin D. B., 1924, *ApJ*, 60, 22
- Madhusudhan N., 2012, *ApJ*, 758, 36
- Madhusudhan N., Winn J. N., 2009, *ApJ*, 693, 784
- Madhusudhan N. et al., 2011, *Nature*, 469, 64
- Mallon M. et al., 2015, *A&A*, 583, A138
- Mancini L. et al., 2013, *MNRAS*, 430, 2932
- Mancini L. et al., 2014, *MNRAS*, 443, 2391
- Mancini L., Kemmer J., Southworth J., Bott K., Molliere P., Ciceri S., Chen G., Henning Th., 2016, preprint ([arXiv:1603.08031](https://arxiv.org/abs/1603.08031))
- Mandel K., Agol E., 2002, *ApJ*, 580, L171
- Mandell A. M., Haynes K., Sinukoff E., Madhusudhan N., Burrows A., Deming D., 2013, *ApJ*, 779, 128
- Mandushev G. et al., 2007, *ApJ*, 667, L195
- Maness H. L., Marcy G. W., Ford E. B., Hauschildt P. H., Shreve A. T., Basri G. B., Butler R. P., Vogt S. S., 2007, *PASP*, 119, 90
- Markwardt C. B., 2009, in Bohlender D. A., Durand D., Dowler P., eds, *ASP Conf. Ser. Vol. 411, Astronomical Data Analysis Software and Systems XVIII*. Astron. Soc. Pac., San Francisco, p. 251
- Matsakos T., Uribe A., Königl A., 2015, *A&A*, 578, A6
- Maxted P. F. L. et al., 2013, *PASP*, 125, 48
- Mislis D., Schröter S., Schmitt J. H. M. M., Cordes O., Reif K., 2010, *A&A*, 510, A107
- Morton D. C., 1991, *ApJS*, 77, 119
- Morton D. C., 2000, *ApJS*, 130, 403
- Moses J. I. et al., 2013, *ApJ*, 777, 34
- Moutou C. et al., 2011, *A&A*, 533, A113
- Moya A., Bouy H., Marchis F., Vicente B., Barrado D., 2011, *A&A*, 535, A110
- Murgas F., Pallé E., Zapatero Osorio M. R., Nortmann L., Hoyer S., Cabrera-Lavers A., 2014, *A&A*, 563, A41
- Narita N., Sato B., Hirano T., Winn J. N., Aoki W., Tamura M., 2010, *PASJ*, 62, 653
- Nascimbeni V., Piotto G., Bedin L. R., Damasso M., Malavolta L., Borsato L., 2011, *A&A*, 532, A24
- Nascimbeni V., Piotto G., Pagano I., Scandariato G., Sani E., Fumana M., 2013, *A&A*, 559, A32
- Nelder J. A., Mead R., 1965, *Comput. J.*, 7, 308
- Nelson B., Davis W. D., 1972, *ApJ*, 174, 617
- Nichols J. D. et al., 2015, *ApJ*, 803, 9
- Nikolov N. et al., 2014, *MNRAS*, 437, 46
- Noyes R. W., Hartmann L. W., Baliunas S. L., Duncan D. K., Vaughan A. H., 1984, *ApJ*, 279, 763
- O'Donovan F. T. et al., 2006, *ApJ*, 651, L61
- O'Donovan F. T., Charbonneau D., Harrington J., Madhusudhan N., Seager S., Deming D., Knutson H. A., 2010, *ApJ*, 710, 1551
- O'Rourke J. G. et al., 2014, *ApJ*, 781, 109
- Oshagh M., Santos N. C., Boisse I., Boué G., Montalto M., Dumusque X., Haghighipour N., 2013, *A&A*, 556, A19
- Oshagh M., Santos N. C., Ehrenreich D., Haghighipour N., Figueira P., Santerne A., Montalto M., 2014, *A&A*, 568, A99
- Pál A., Sárneczky K., Szabó G. M., Szing A., Kiss L. L., Mező G., Regály Z., 2011, *MNRAS*, 413, L43
- Pearson K. A., Turner J. D., Sagan T. G., 2014, *New Astron.*, 27, 102
- Pollacco D. L. et al., 2006, *PASP*, 118, 1407
- Pont F., Zucker S., Queloz D., 2006, *MNRAS*, 373, 231
- Pont F. et al., 2010, *MNRAS*, 402, L1
- Popper D. M., 1984, *AJ*, 89, 132
- Popper D. M., Etzel P. B., 1981, *AJ*, 86, 102
- Press W. H., Teukolsky S. A., Vetterling W. T., Flannery B. P., 1992, *Numerical Recipes in FORTRAN. The Art of Scientific Computing*. Cambridge Univ. Press, Cambridge
- Ranjan S., Charbonneau D., Désert J.-M., Madhusudhan N., Deming D., Wilkins A., Mandell A. M., 2014, *ApJ*, 785, 148
- Rappaport S. et al., 2012, *ApJ*, 752, 1
- Rappaport S., Barclay T., DeVore J., Rowe J., Sanchis-Ojeda R., Still M., 2014, *ApJ*, 784, 40
- Rauer H. et al., 2010, *AJ*, 139, 53
- Ribas I., Font-Ribera A., Beaulieu J.-P., 2008, *ApJ*, 677, L59
- Ricci D. et al., 2015, *PASP*, 127, 143

- Rogers J. C., Apai D., López-Morales M., Sing D. K., Burrows A., 2009, *ApJ*, 707, 1707
- Rogers J., López-Morales M., Apai D., Adams E., 2013, *ApJ*, 767, 64
- Rossiter R. A., 1924, *ApJ*, 60, 15
- Sada P. V., Ramón-Fox F. G., 2016, *PASP*, 128, 024402
- Sada P. V. et al., 2012, *PASP*, 124, 212
- Safronov V. S., 1972, *Evolution of the Protoplanetary Cloud and Formation of the Earth and Planets*. Keter Publishing House, Jerusalem, p. 212
- Sansonetti J. E., 2005, *J. Phys. Chem. Ref. Data*, 34, 1559
- Schlawin E., Zhao M., Teske J. K., Herter T., 2014, *ApJ*, 783, 5
- Schröter S., Schmitt J. H. M. M., Müller H. M., 2012, *A&A*, 539, A97
- Schwarz G., 1978, *Ann. Stat.*, 6, 461
- Scuderi L. J., Dittmann J. A., Males J. R., Green E. M., Close L. M., 2010, *ApJ*, 714, 462
- Seager S., 2011, *Exoplanets*. Univ. Arizona Press, Tuscan, AZ
- Seager S., Sasselov D. D., 2000, *ApJ*, 537, 916
- Shabram M., Fortney J. J., Greene T. P., Freedman R. S., 2011, *ApJ*, 727, 65
- Shporer A., Tamuz O., Zucker S., Mazeh T., 2007, *MNRAS*, 376, 1296
- Shporer A., Mazeh T., Pont F., Winn J. N., Holman M. J., Latham D. W., Esquerdo G. A., 2009, *ApJ*, 694, 1559
- Simpson E. K. et al., 2011, *MNRAS*, 414, 3023
- Sing D. K., Vidal-Madjar A., Désert J.-M., Lecavelier des Etangs A., Ballester G., 2008, *ApJ*, 686, 658
- Sing D. K. et al., 2011, *MNRAS*, 416, 1443
- Sing D. K. et al., 2013, *MNRAS*, 436, 2956
- Sing D. K. et al., 2015, *MNRAS*, 446, 2428
- Sing D. K. et al., 2016, *Nature*, 529, 59
- Smith A. M. S., Anderson D. R., Skillen I., Collier Cameron A., Smalley B., 2011, *MNRAS*, 416, 2096
- Smith A. M. S. et al., 2012, *AJ*, 143, 81
- Snellen I. A. G., de Mooij E. J. W., Albrecht S., 2009, *Nature*, 459, 543
- Sokov E. N. et al., 2012, *Astron. Lett.*, 38, 180
- Southworth J., 2008, *MNRAS*, 386, 1644
- Southworth J., 2010, *MNRAS*, 408, 1689
- Southworth J., 2011, *MNRAS*, 417, 2166
- Southworth J., 2012, *MNRAS*, 426, 1291
- Southworth J., Maxted P. F. L., Smalley B., 2004a, *MNRAS*, 349, 547
- Southworth J., Maxted P. F. L., Smalley B., 2004b, *MNRAS*, 351, 1277
- Southworth J., Wheatley P. J., Sams G., 2007a, *MNRAS*, 379, L11
- Southworth J., Bruntt H., Buzasi D. L., 2007b, *A&A*, 467, 1215
- Southworth J., Bruni I., Mancini L., Gregorio J., 2012a, *MNRAS*, 420, 2580
- Southworth J., Mancini L., Maxted P. F. L., Bruni I., Tregloan-Reed J., Barbieri M., Ruocco N., Wheatley P. J., 2012b, *MNRAS*, 422, 3099
- Southworth J. et al., 2015, *MNRAS*, 447, 711
- Sozzetti A. et al., 2009, *ApJ*, 691, 1145
- Sozzetti A. et al., 2015, *A&A*, 575, L15
- Stempels H. C., Collier Cameron A., Hebb L., Smalley B., Frandsen S., 2007, *MNRAS*, 379, 773
- Stevenson K. B. et al., 2012, *ApJ*, 755, 9
- Stevenson K. B., Bean J. L., Seifahrt A., Désert J.-M., Madhusudhan N., Bergmann M., Kreidberg L., Homeier D., 2014a, *AJ*, 147, 161
- Stevenson K. B., Bean J. L., Madhusudhan N., Harrington J., 2014b, *ApJ*, 791, 36
- Swain M. et al., 2013, *Icarus*, 225, 432
- Szabó G. M. et al., 2010, *A&A*, 523, A84
- Teske J. K., Turner J. D., Mueller M., Griffith C. A., 2013, *MNRAS*, 431, 1669
- Teske J. K., Cunha K., Smith V. V., Schuler S. C., Griffith C. A., 2014, *ApJ*, 788, 39
- Tinetti G., Deroo P., Swain M. R., Griffith C. A., Vasisth G., Brown L. R., Burke C., McCullough P., 2010, *ApJ*, 712, L139
- Todorov K., Deming D., Harrington J., Stevenson K. B., Bowman W. C., Nymeyer S., Fortney J. J., Bakos G. A., 2010, *ApJ*, 708, 498
- Todorov K. O. et al., 2012, *ApJ*, 746, 111
- Torres G., 2007, *ApJ*, 671, L65
- Torres G., Winn J. N., Holman M. J., 2008, *ApJ*, 677, 1324
- Turner J. D. et al., 2013, *MNRAS*, 428, 678
- Turner J. D., Christie D., Arras P., Johnson R. E., Schmidt C., 2016, preprint ([arXiv:1603.01229](https://arxiv.org/abs/1603.01229))
- van Werkhoven T. I. M., Brogi M., Snellen I. A. G., Keller C. U., 2014, *A&A*, 561, A3
- Vidal-Madjar A., Lecavelier des Etangs A., Désert J.-M., Ballester G. E., Ferlet R., Hébrard G., Mayor M., 2003, *Nature*, 422, 143
- Vidal-Madjar A. et al., 2004, *ApJ*, 604, L69
- Vidal-Madjar A., Lecavelier des Etangs A., Désert J.-M., Ballester G. E., Ferlet R., Hébrard G., Mayor M., 2008, *ApJ*, 676, L57
- Vidal-Madjar A. et al., 2013, *A&A*, 560, A54
- Vidotto A. A., Jardine M., Helling C., 2010, *ApJ*, 722, L168
- Vidotto A. A., Llama J., Jardine M., Helling C., Wood K., 2011a, *Astron. Nachr.*, 332, 1055
- Vidotto A. A., Jardine M., Helling C., 2011b, *MNRAS*, 411, L46
- Vidotto A. A., Jardine M., Helling C., 2011c, *MNRAS*, 414, 1573
- von Braun K. et al., 2012, *ApJ*, 753, 171
- von Essen C. et al., 2014, *A&A*, 561, A48
- von Essen C., Mallonn M., Albrecht S., Antoci V., Smith A. M. S., Dreizler S., Strassmeier K. G., 2015, *A&A*, 584, A75
- Wheatley P. J. et al., 2010, preprint ([arXiv:1004.0836](https://arxiv.org/abs/1004.0836))
- Wilson P. A. et al., 2015, *MNRAS*, 450, 192
- Winn J. N., 2011, in Sozzetti A., Lattanzi M. G., Boss A. P., eds, *Proc. IAU Symp. 276, The Astrophysics of Planetary Systems: Formation, Structure, and Dynamical Evolution*. Kluwer, Dordrecht, p. 230
- Winn J. N. et al., 2007, *AJ*, 134, 1707
- Winn J. N. et al., 2008a, *ApJ*, 682, 1283
- Winn J. N. et al., 2008b, *ApJ*, 683, 1076
- Winn J. N. et al., 2010, *ApJ*, 718, 575
- Wright J. T. et al., 2007, *ApJ*, 657, 533
- Wright J. T. et al., 2011, *PASP*, 123, 412
- Zellem R. T. et al., 2014, *ApJ*, 790, 53
- Zellem R. T. et al., 2015, *ApJ*, 810, 11
- Zhao M., Monnier J. D., Swain M. R., Barman T., Hinkley S., 2012, *ApJ*, 744, 122

SUPPORTING INFORMATION

Additional Supporting Information may be found in the online version of this article:

Table 3. Photometry of all our light curves.

Table 15. Results of the transit timing analysis.¹

Table 16. R_p/R_* and central wavelength λ_{eff} from this paper and previous literature for all targets (<http://www.mnras.oxfordjournals.org/lookup/suppl/doi:10.1093/mnras/stw574/-/DC1>).

Please note: Oxford University Press is not responsible for the content or functionality of any supporting materials supplied by the authors. Any queries (other than missing material) should be directed to the corresponding author for this article.

¹Lunar and Planetary Laboratory, University of Arizona, Tucson, AZ 85721, USA

²Department of Astronomy, University of Virginia, Charlottesville, VA 22904, USA

³Steward Observatory, University of Arizona, Tucson, AZ 85721, USA

⁴Department of Astronomy, University of Wisconsin, Madison, WI 53706, USA

⁵Department of Physics and Astronomy, University of Toledo, Toledo, OH 43606, USA

⁶Kitt Peak National Observatory, National Optical Astronomy Observatory, Tucson, AZ 85719, USA

⁷Institut für Quantenoptik, Leibniz Universität Hannover, D-30167 Hannover, Germany

⁸Department of Physics and Astronomy, University of California, Irvine, CA 92687, USA

⁹Space Telescope Science Institute, Baltimore, MD 21218, USA

This paper has been typeset from a \LaTeX file prepared by the author.